On-orbit calibration of the Suomi National Polar-Orbiting Partnership Visible Infrared Imaging Radiometer Suite for ocean color applications

Robert E. Eplee, Jr.,[1,*] Kevin R. Turpie,[2] Gerhard Meister,[3] Frederick S. Patt,[1] Bryan A. Franz,[3] and Sean W. Bailey[4]

[1]Science Applications International Corporation, 4600 Powdermill Road, Suite 400, Beltsville, Maryland 20705, USA

[2]Joint Center for Earth Systems Technology, University of Maryland, Baltimore County, Catonsville, Maryland 21250, USA

[3]Ocean Ecology Branch, Code 616, NASA Goddard Space Flight Center, Greenbelt, Maryland 20771, USA

[4]FutureTech Corporation, 7307 Hanover Parkway, Suite D, Greenbelt, Maryland 20770, USA

*Corresponding author: Robert.E.Eplee@nasa.gov

Received 24 November 2014; revised 22 January 2015; accepted 22 January 2015; posted 29 January 2015 (Doc. ID 228396); published 5 March 2015

The NASA Ocean Biology Processing Group (OBPG) developed two independent calibrations of the Suomi National Polar-Orbiting Partnership (SNPP) Visible Infrared Imaging Radiometer Suite (VIIRS) moderate resolution reflective solar bands using solar diffuser measurements and lunar observations, and implemented a combined solar- and lunar-based calibration to track temporal changes in radiometric response of the instrument. Differences between the solar and lunar data sets have been used to identify issues and verify improvements in each. Linearization of the counts-to-radiance conversion yields a more consistent calibration at low radiance levels. Correction of a recently identified error in the VIIRS solar unit vector coordinate frame has been incorporated into the solar data and diffuser screen transmission functions. Temporal trends in the solar diffuser stability monitor data have been evaluated and addressed. Fits to the solar calibration time series show mean residuals per band of 0.067%–0.17%. Periodic residuals in the VIIRS lunar data are confirmed to arise from a wavelength-dependent libration effect for the sub-spacecraft point in the output of the U.S. Geological Survey Robotic Lunar Observatory photometric model of the Moon. Temporal variations in the relative spectral responses for each band have been assessed, and significant impact on band M1 (412 nm) lunar data has been identified and rectified. Fits to the lunar calibration time series, incorporating sub-spacecraft point libration corrections, show mean residuals per band of 0.069%–0.20%. Lunar calibrations have been used to adjust the solar-derived radiometric corrections for bands M1, M3, and M4. After all corrections, the relative differences in the solar and lunar calibrations for bands M1–M7 are 0.093%–0.22%. The OBPG has achieved a radiometric stability for the VIIRS on-orbit calibration that is commensurate with those achieved for SeaWiFS and Aqua MODIS, supporting the incorporation of VIIRS data into the long-term NASA ocean color data record. © 2015 Optical Society of America

OCIS codes: (280.0280) Remote sensing and sensors; (280.4788) Optical sensing and sensors; (280.4991) Passive remote sensing; (010.1690) Color; (010.5630) Radiometry; (120.0280) Remote sensing and sensors.

http://dx.doi.org/10.1364/AO.54.001984

1. Introduction

The Suomi National Polar-Orbiting Partnership (SNPP) Visible Infrared Imaging Radiometer Suite (VIIRS) was launched into an 824 km sun-synchronous

1559-128X/15/081984-23$15.00/0
© 2015 Optical Society of America

polar orbit with a node crossing time of 13:30 on 28 October 2011. VIIRS is a 22-band scanning filter radiometer whose design heritage is SeaWiFS (rotating telescope with half-angle mirror) and MODIS (focal plan layout, solar diffuser, solar diffuser screen, solar diffuser stability monitor). The primary calibration responsibility for VIIRS resides with the NOAA National Environmental Satellite, Data, and Information Service (NESDIS), Center for Satellite Applications and Research (STAR) VIIRS Sensor Data Record (SDR) Calibration Working Group (CWG) [1–3], with support provided by the NASA VIIRS Characterization Support Team (VCST) [4,5]. Reflective solar band measurements of the solar diffuser began shortly after a stable orbit was acquired. VIIRS acquired its first image on its warm focal plane when its nadir door was opened on 21 November 2011; the instrument's cooled focal planes were turned on 20 January 2012. Early in the VIIRS on-orbit operations, the near-infrared (NIR) Degradation Anomaly was observed, where tungsten oxide contamination of mirrors in the rotating telescope assembly was found to be causing a rapid decrease in mirror reflectance for the near-infrared and shortwave-infrared spectral region [6–8]. The operational configuration of VIIRS was changed frequently while the anomaly was under investigation. Continuous operation of the instrument began on 2 January 2012 in preparation for the first lunar calibration, and the instrument operations have been relatively stable since that time.

One challenge of climate change research is to discern small secular trends in geophysical processes that have comparatively large daily, seasonal, annual, or longer-scale periodic signals. Accordingly, a primary goal of the NASA Ocean Biology Processing Group (OBPG) is to produce a climate data record for ocean color data [9]: a time series of measurements of sufficient length, consistency, and continuity that will allow determinations of climate variability and change [10]. This endeavor requires that remote sensing data be collected from satellite instruments with long-term radiometric stability, where the radiometric uncertainty in the data is less than the magnitude of the possible climate change signal. For ocean color data, the radiometric requirements are 5% absolute and 1% relative accuracies for water-leaving radiances [11]. The 1% relative accuracy requirement on water-leaving radiances translates into a 0.1% long-term radiometric stability requirement for top-of-the-atmosphere (TOA) radiances [12] over the time scales for which the relative accuracy goal is to be met. The OBPG was able to achieve this level of stability over the lifetime of SeaWiFS [13]. The long-term radiometric stability requirements for ocean color sensors necessitate the implementation of robust on-orbit calibration procedures for the reflective solar bands of these instruments. The primary components of these calibration procedures are solar calibrations, through observations of sunlight reflected by a solar diffuser, and lunar calibrations. Solar diffuser observations provide frequent opportunities (once per orbit to once per day or less frequent observations), while lunar observations provide 8–9 monthly calibration opportunities per year. Uncertainties in the sensor calibration and atmospheric correction algorithm necessitate a vicarious calibration of the sensor/atmospheric correction algorithm system to meet the absolute accuracy requirements [14].

While the production of climate quality ocean color data products places stringent requirements on the on-orbit calibration of the reflective solar bands, there are issues with the NOAA operational calibration of VIIRS for these bands [15]. Since the SNPP VIIRS launch, the OBPG has implemented an in-house on-orbit calibration capability for VIIRS to meet the more exacting calibration needs of NASA's ocean color applications [16,17]. Recently, NOAA NESDIS/STAR has implemented its own in-house calibration for ocean color data processing [18–21].

In this paper, we detail the specific improvements to the VIIRS on-orbit calibration implemented by the OBPG for the reflective solar bands, specifically the calibration of visible and near-infrared bands M1–M7, whose characteristics are listed in Table 1. This effort is being carried out in cooperation with VCST and with the U.S. Geological Survey (USGS) Robotic Lunar Observatory (ROLO) program. For clarity of reference, the current VIIRS calibration presented in this paper is referred to as the OBPG Reprocessing R2014.0 calibration [22], while the previous calibration is referred to as the OBPG Reprocessing R2013.1 calibration [17,22].

Solar calibration is the first method for monitoring the on-orbit radiometric performance of the reflective solar bands. The VIIRS solar diffuser (SD) is a Spectralon panel placed behind a solar attenuation screen. VIIRS observes sunlight reflected by the SD once per orbit as the spacecraft crosses the South Pole, moving from the Earth's shadow into sunlight [23,24]. To yield the actual change in instrument response, the SD time series must be corrected by the solar diffuser stability monitor (SDSM)-derived change in the bidirectional reflectance distribution function (BRDF) of the SD. The SDSM is an 8-channel ratioing radiometer with wavelengths corresponding to VIIRS bands M1–M7 and a reference channel at 935 nm. The SDSM sequentially observes the Sun (through an attenuation screen) and the SD to monitor changes in the diffuser BRDF over time. The change in the VIIRS radiometric sensitivity over time is computed from the SD data (the F-factor or radiometric gain), corrected for the change in the diffuser BRDF (the H-factor). Because of the rapid change in the diffuser BRDF, the OBPG has performed an in-depth evaluation of the BRDF correction provided by the SDSM measurements. The solar calibration procedure yields a calibration of the instrument on a per-band, per-detector basis for high and low gain states and the two sides of the half-angle mirror. It was recently discovered that the solar unit vectors used for processing the SD and SDSM data were reported in the inertial true-of-date reference frame

Table 1. VIIRS Reflective Solar Bands[a]

VIIRS Band	SDSM Channel	Band Center (nm)	Bandwidth (nm)	Single/Dual Gain	Spatial Resolution at Nadir (m)	Focal Plane
M1	C1	412	20	DG	750	VNIR
M2	C2	445	18	DG	750	VNIR
M3	C3	488	20	DG	750	VNIR
M4	C4	555	20	DG	750	VNIR
I1		640	80	SG	375	VNIR
M5	C5	672	20	DG	750	VNIR
M6	C6	746	15	SG	750	VNIR
I2		865	41	SG	375	VNIR
M7	C7	865	41	DG	750	VNIR
	C8	935				
M8		1240	20	SG	750	SWIR
M9		1378	15	SG	750	SWIR
I3		1610	60	SG	375	SWIR
M10		1610	60	SG	750	SWIR
M11		2250	50	SG	750	SWIR

[a]The table shows the characteristics of the reflective solar bands of VIIRS, along with the centers of the SDSM channels. This paper addresses the calibration of bands M1–M7, making use of the SDSM channels. SDSM channels 1–7 correspond to VIIRS bands M1–M7, while channel 8 does not have a corresponding VIIRS band.

rather than the expected J2000 (the standard reference frame of 1 January 2000) reference frame. Accordingly, corrections to the solar unit vectors have been developed and incorporated into the solar data. VCST has used these corrected unit vectors and on-orbit yaw maneuver and flight data collected over the mission to generate a revised set of transmission functions for the solar attenuation screens which yield a more accurate characterization of the transmission at a finer angular resolution over an expanded angular range [25] than was provided by the previous transmission functions.

Lunar calibration is the second method for monitoring the radiometric response of the reflective solar bands on orbit. The spacecraft is rolled once per month to observe the Moon through the space view at a nominal phase angle of −51° [23,24]. Since band M1 (412) has a large out-of-band response at red wavelengths, the NIR Degradation Anomaly causes changes in the relative spectral responses (RSRs) for this band over time [26,27]. Accordingly, time-dependent, or modulated, RSRs are required to properly monitor the radiometric response of this band using lunar data. Disk-integrated irradiances are computed from the resulting lunar images. These lunar irradiances are compared with the USGS ROLO photometric model of the Moon [28,29] to yield a time series of ratios of instrument measurements to model predictions, which represent the temporal change in the radiometric response of the instrument. An in-depth analysis of periodic residuals in the lunar time series shows that the residuals arise from wavelength-dependent sub-spacecraft point libration effects in the output of the ROLO model. The lunar calibration procedure yields a calibration of the instrument on a per-band basis for the two sides of the half-angle mirror, while the responses of the individual detectors are unresolved. Changes in lunar observing geometry over the course of a year limit the number of lunar observations to 8–9 per year.

Unlike heritage instruments, VIIRS observes the solar diffuser and the Moon at the same angle of incidence on its half-angle mirror. Accordingly, the OBPG used a direct comparison of solar and lunar calibrations to minimize uncertainties in the derived instrument response over time. The understanding of the VIIRS on-orbit calibration performance is continuing to evolve as more on-orbit calibration data becomes available [16,17]. The culmination of improvements in the solar and lunar calibration time series, as described in this paper, have reduced the differences between the two calibration time series to within 0.22%. The OBPG has observed statistically significant trends between the improved solar and lunar time series for bands M1, M3, and M4. Since measurements of the Moon are more stable over time than are measurements of the Sun via a continuously changing solar diffuser [30], the OBPG corrected the solar time series for the extraneous trends observed relative to the Moon. The resulting calibration improved the agreement between the ocean surface reflectance and chlorophyll time series observed by VIIRS and the long-term NASA ocean color data record established with SeaWiFS and Aqua MODIS.

Once long-term radiometric trends have been removed from the instrument on-orbit calibration, TOA radiances must be vicariously calibrated to minimize any remaining radiometric biases [14]. The OBPG has vicariously calibrated the visible bands of VIIRS (bands M1–M5) against in-water measurements of the light field measured by the Marine Optical BuoY (MOBY) [31,32]. Band M6 (746 nm) has been vicariously calibrated relative to band M7 (865 nm) so that the atmospheric correction algorithm retrieves the expected aerosol types and optical depths for open ocean scenes [14,33]. Vicarious calibration minimizes biases in the instrument

calibration and uncertainties in the atmospheric correction algorithm.

The procedures for on-orbit calibration developed by the OBPG make full use of the mission-long solar and lunar calibration time series for VIIRS and the OBPG's capabilities of frequent ocean data reprocessing [22], rather than the automated on-orbit calibration approach adopted by the NOAA VIIRS SDR CWG for the NOAA Interface Data Processing System [34] or the VIIRS SDR update approach using F-factor ratios adopted by NOAA NESDIS/STAR for NOAA ocean data processing [20]. In this paper, we will discuss the details of the OBPG approach to VIIRS calibration. For plots of solar and lunar radiometric trends shown in this paper, the time series are typically normalized to the first observation in the series. In the final discussion section (Section 9), we will bring together in one place the various equations required to derive the on-orbit calibration of VIIRS. The end result of the OBPG on-orbit calibration analyses is a calibration lookup table and set of vicarious gains for use in NASA ocean color data processing from the start of continuous VIIRS operations on 2 January 2012.

2. Prelaunch Calibration

The prelaunch calibration of VIIRS yielded quadratic counts-to-radiance conversion coefficients for the reflective solar bands [3]. VCST provided the OBPG with the counts-to-radiance conversion characterization data. For calibration purposes, VIIRS observes radiance reflected by the solar diffuser [4]:

$$L_{\mathrm{sd}}(\lambda,t) = c_0(\lambda,t) + c_1(\lambda,t)dn_{\mathrm{sd}}(\lambda,t) + c_2(\lambda,t)dn_{\mathrm{sd}}^2(\lambda,t), \tag{1}$$

where

$c_i \equiv$ counts-to-radiance conversion coefficients,
$dn_{sd} \equiv$ dark-subtracted counts of the solar diffuser observations.

For VIIRS, the dark count is determined on a per-four scan line basis from the space view. The instrument rotates through both sides of the half-angle mirror and both high and low gains in four successive scans.

During the initial development of its VIIRS calibration capability, the OBPG reanalyzed the characterization data over the range of expected TOA radiances for each band (shown in Table 2), computing linear counts-to-radiance conversion coefficients c_1 for each detector and gain. The dark-subtracted counts dn_{sd} for zero illumination should be zero, so calibration consistency at low radiance levels requires c_0 to be zero. This reanalysis effectively sets c_2 to zero, as well, since the nonlinear region of the response is at radiances higher than the expected maximum observed over clouds. So, the reanalyzed solar radiance observed by VIIRS becomes

Table 2. VIIRS TOA Radiances Ranges[a]

		High Gain		Low Gain	
Band	λ(nm)	$L_{\min}$	$L_{\max}$	$L_{\min}$	$L_{\max}$
M1	412	30	135	135	615
M2	445	26	127	127	687
M3	488	22	107	107	702
M4	555	12	78	78	667
M5	672	8.6	59	59	651
M6[b]	746	5.3	41		
M7	865	3.4	29	29	349

[a]The range of expected TOA radiances are provided for bands M1–M7 [3]. For the dual gain bands (M1–M5 and M7), the radiance ranges for both high and low gains are provided. The radiance units are $\mathrm{W\,m^{-2}\,sr^{-1}\,\mu m^{-1}}$.
[b]M6 is a single-gain band.

$$L_{\mathrm{sd}}(\lambda,t) = c_1(\lambda,t)dn_{\mathrm{sd}}(\lambda,t). \tag{2}$$

This equation is a linear function of counts, but it is dual gain. Ocean observations are made at high gain, while cloud observations are made at low gain. As noted above, the solar calibrations are performed at both high and low gains, while the scheduled lunar calibrations are performed at high gain. For ocean color processing, vicarious calibration corrects for any biases in the counts-to-radiance conversion for the VIIRS TOA radiances.

Since the time of the OBPG reanalysis, the NOAA VIIRS SDR CWG has also improved the SDR performance at low radiance levels by setting the counts-to-radiance conversion coefficients c_0 to zero and reanalyzing the c_1 and c_2 coefficients [35]. The NOAA reanalysis results were implemented in NOAA operational VIIRS data processing for bands M1–M7, effective 1 May 2014.

3. Solar Calibration

VIIRS views sunlight reflected by the solar diffuser as the SNPP spacecraft passes over the South Pole, moving from the Earth's shadow into the Sun. VIIRS SD observations provide the monitor for the radiometric response of the instrument, while the ratio of SDSM diffuser observations to SDSM solar observations provide the monitor for changes in the diffuser BRDF.

Geometric corrections that are applied to the solar calibration data include instrument–Sun distances, transmission functions for the SD and SDSM attenuation screens (through solar illumination angles on the screens), and the diffuser BRDF (through solar illumination angles on the diffuser). The prelaunch characterizations of the screen transmission functions and diffuser BRDF were performed over a limited range of observations. These functions have been evaluated on orbit through spacecraft yaw maneuvers [24], with resulting updates to the transmission functions and diffuser BRDF [36]. The transmission functions and diffuser BRDF were updated yet again incorporating the corrected solar unit vectors and using additional yaw maneuver and flight data

collected over the mission [25]. The solar calibration data discussed in this analysis extends from the start of the mission through the SDSM measurement obtained on 16 July 2014.

A. Solar Diffuser Degradation

The SDSM time series are used to monitor the changes in the diffuser BRDF. The BRDF history function is the ratio of the solar diffuser measurement to the direct solar measurement made by the SDSM [4]:

$$h(\lambda,t) = \frac{\langle dn_{\mathrm{sd}}(\lambda,t)\rangle}{\langle dn_{\mathrm{sun}}(\lambda,t)\rangle}\frac{\cos(\phi(t))\tau_{\mathrm{sdsm}}(\lambda)}{\tau_{\mathrm{sds}}(\lambda)\mathrm{BRDF}(\lambda,t_o)\Omega_{\mathrm{sdsm}}}, \quad (3)$$

where

$dn_{\mathrm{sd}} \equiv$ dark-subtracted SDSM counts of SD observations,
$dn_{\mathrm{sun}} \equiv$ dark-subtracted SDSM counts of solar observations,
$\Omega_{\mathrm{sdsm}} \equiv$ cone angle of the SDSM view of the solar diffuser,
$\lambda \equiv$ VIIRS band,
$t \equiv$ time of the observation,
$t_o \equiv$ reference time for the instrument trends,
$\phi \equiv$ incidence angle of the Sun on the solar diffuser,
$\tau_{\mathrm{sds}} \equiv$ transmittance of the solar diffuser screen,
$\tau_{\mathrm{sdsm}} \equiv$ transmittance of the SDSM screen.

In this analysis, the dark-subtracted counts for both the solar diffuser and direct solar observations are averaged over five samples per scan and for the unobstructed scans in each observation. The time-dependent BRDF correction, the H-factor, is

$$H(\lambda,t) = \frac{h(\lambda,t)}{h(\lambda,t_0)}. \quad (4)$$

The SDSM trends over time are subject to measurement noise and other calibration artifacts. Historically, the diffuser BRDF at 935 nm is assumed to be invariant over short periods of time [37,38], so this channel (SDSM channel 8) is used to normalize the SDSM trends to correct for these artifacts. The SDSM time series for channels 1–7, normalized by channel 8, are used to correct the band M1–M7 solar calibration time series for changes in the diffuser BRDF. Figure 1 shows the SDSM trends.

Since VIIRS does not have a diffuser door, the rate of diffuser BRDF degradation on orbit is comparable to that observed for Terra MODIS after its diffuser door failed in the open position [39]. The observed temporal trend in SDSM channel 8, shown in Fig. 2, is inconsistent with the assumption that the diffuser BRDF is invariant at 935 nm. Comparison of the channel 8 time series [see Fig. 2(a)] with the time series of solar incidence angles [Fig. 2(c)] shows correlations between the channel 8 data and the solar incidence angles. These correlations could arise from errors due to time dependencies in the transmission functions of the SD and SDSM screens. These correlations are also present in SDSM channels 1–7. So, in order to correct for the transmission function errors in channels 1–7 without imposing the temporal trend of channel 8 onto the shorter wavelength channels, the OBPG has calculated a detrended channel 8 H-factor.

To detrend the channel 8 time series, the OBPG has fit the SDSM data with an exponential function of time plus a linear function of the solar incidence angle (ϕ):

$$f(\phi,t) = A_0 - A_1[1 - e^{-A_2(t-t_0)}] + A_3\phi, \quad (5)$$

where A_i are the fitted values of the function. The fit to the channel 8 time series is shown in Fig. 2(a). The exponential function of time is used to detrend the channel 8 time series for the temporal drift:

$$K_{c8}(t) = A_0 - A_1[1 - e^{-A_2(t-t_0)}]. \quad (6)$$

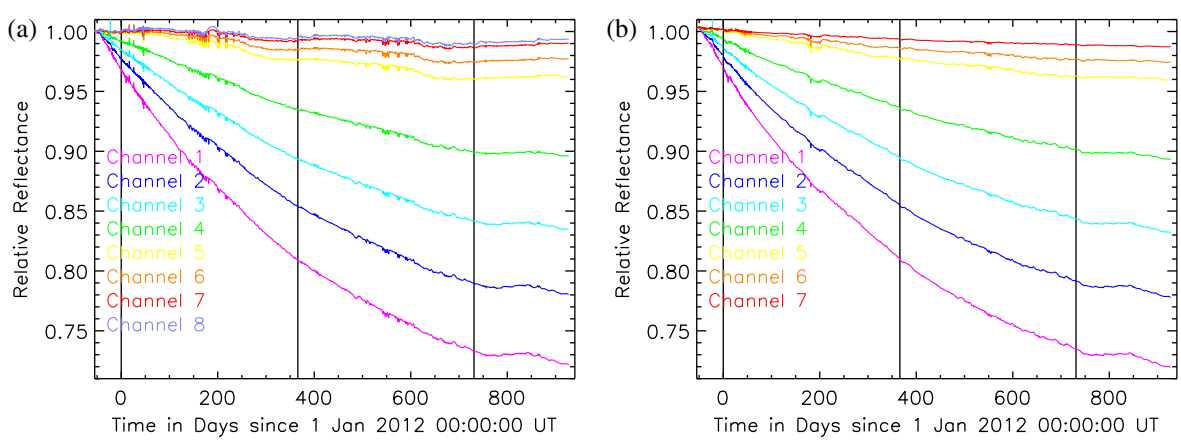

Fig. 1. Solar diffuser stability monitor time series. (a) The trends for channels 1–8. (b) The trends for channels 1–7 after normalization by the detrended channel 8. The normalized series shows the change in diffuser BRDF over time. The H-factor time series is interpolated to the time basis of the solar calibration data.

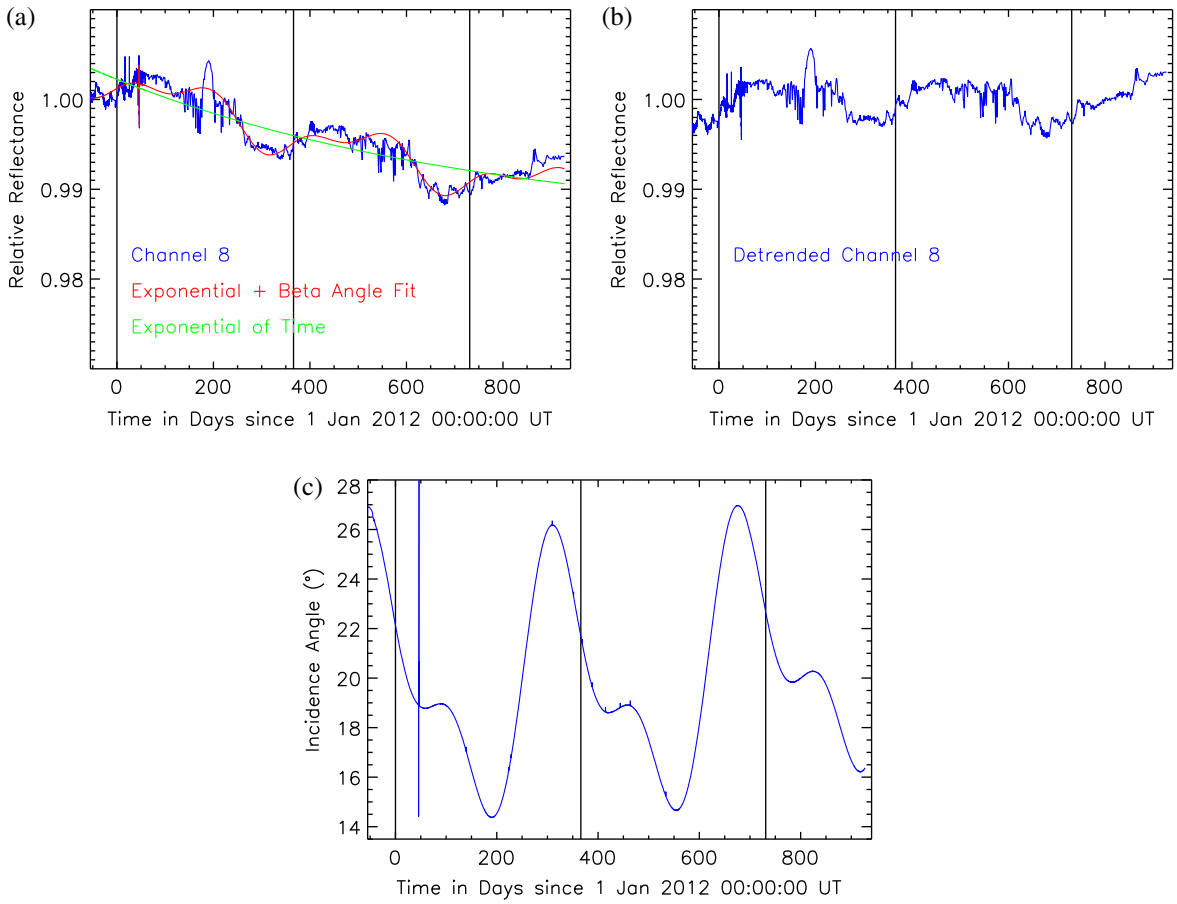

Fig. 2. Solar diffuser stability monitor channel 8 time series. (a) Channel 8 time series with fits for time and solar incidence angle. (b) Channel 8 time series after detrending by the exponential of time. (c) The solar incidence angle time series. The detrended channel 8 time series provides the optimum normalization for SDSM channels 1–7.

Since the fit to channel 8 is performed to derive the time dependence in the time series, the behavior of the solar incidence angle is captured by a linear function with sufficient fidelity to allow the temporal trend to be determined, as shown in Fig. 2(b). The detrended channel 8 H-factor becomes

$$HD_{c8}(t) = \frac{1}{K_{c8}(t)} \frac{h_{c8}(t)}{h_{c8}(t_0)}. \tag{7}$$

The BRDF corrections (the H-factors normalized by channel 8) for SDSM channels 1–7 become

$$NH(\lambda, t) = \frac{H(\lambda, t)}{HD_{c8}(t)} = K_{c8}(t) \frac{h(\lambda, t)}{h(\lambda, t_0)} \frac{h_{c8}(t_0)}{h_{c8}(t)}. \tag{8}$$

Figure 1(b) shows that the BRDF degradation decreases with increasing wavelength, as has been reported for VIIRS [19] and as is expected from heritage experience with solar diffusers on orbit [13,39–41]. The BRDF degradation is a result of exposure of the diffuser to ultraviolet light from the Sun [42].

This analysis has allowed the OBPG to identify three options for normalizing the H-factors that monitor the diffuser BRDF degradation:

(1) Using unnormalized H-factors.
(2) Using H-factors normalized by SDSM channel 8.
(3) Using H-factors normalized by the detrended SDSM channel 8.

These options will be evaluated below as part of the solar diffuser trend analysis and in Section 5 of this paper as part of the solar/lunar calibration comparisons. The optimum approach minimizes the noise in SDSM channels 1–7 without introducing temporal errors into the solar calibration data.

To further minimize artifacts in the SDSM time series that may be introduced into the solar calibration data, the OBPG has examined several methods of trending and/or using the H-factors to correct the solar diffuser measurements for SD degradation. Initial approaches involved smoothing or fitting curves to the H-factors. These approaches tended to either remove real, short-term variations in the SD degradation from the H-factors or to introduce smoothing or fitting artifacts into the F-factors. The OBPG found that the optimum approach is to

interpolate the H-factors to the time basis of the solar observations, then to directly correct the solar data for bands M1–M7 by the interpolated, normalized H-factors for channels 1–7. This approach minimizes short-term fluctuations in SD trends that are simultaneously observed in both the SDSM and SD data. In contrast, the current NOAA operational calibration method smooths the H-factors with time, allowing fluctuations that do not pertain to VIIRS response changes to persist in the F-factor time series.

B. Solar-Derived Radiometric Response Trends

The VIIRS radiometric gain over time (the F-factor, which is dimensionless) is computed from the solar calibration time series. The gain is the ratio of the predicted solar radiance incident on the solar diffuser (L_{pred}) to the actual solar radiance reflected by the diffuser and measured by VIIRS (L_{sd}) [4]:

$$F(\lambda,t) = \mathrm{RVS}(\theta_{\mathrm{sd}},\lambda)\cos(\phi(t))\frac{L_{\mathrm{pred}}(\lambda,t)}{L_{\mathrm{sd}}(\lambda,t)}, \tag{9}$$

where

RVS ≡ response versus scan angle correction, measured prelaunch,
θ_{sd} ≡ angle of incidence of the solar diffuser on the half-angle mirror,
ϕ ≡ incidence angle of the Sun on the solar diffuser.

The predicted solar radiance is

$$L_{\mathrm{pred}}(\lambda,t) = \frac{E_{\mathrm{sun}}(\lambda)}{R_{\mathrm{se}}^2(t)}\tau_{\mathrm{sds}}(\lambda)\mathrm{BRDF}(\lambda,t_0)NH(\lambda,t), \tag{10}$$

where

E_{sun} ≡ solar irradiance at one astronomical unit,
R_{se} ≡ Sun-Earth distance in astronomical units.

The OBPG has implemented the observed solar radiance as a linear function of instrument counts:

$$L_{\mathrm{sd}}(\lambda,t) = c_1(\lambda,t)dn_{\mathrm{sd}}(\lambda,t), \tag{11}$$

where

c_1 ≡ linear counts-to-radiance conversion coefficient,
dn_{sd} ≡ dark-subtracted counts of the solar diffuser observations.

In terms of instrument measurements, the F-factor becomes

$$F(\lambda,t) = \frac{E_{\mathrm{sun}}(\lambda)}{R_{\mathrm{se}}^2(t)}\frac{\mathrm{RVS}(\theta_{\mathrm{sd}},\lambda)\cos(\phi(t))\tau_{\mathrm{sds}}(\lambda)\mathrm{BRDF}(\lambda,t_0)}{c_1(\lambda,t)\langle dn_{\mathrm{sd}}(\lambda,t)\rangle} \times NH(\lambda,t). \tag{12}$$

The dark-subtracted counts of the SD observations are averaged over the 48 samples per scan and the valid scans of each observation for the two gains and two mirror sides.

The OBPG approach to solar calibration data analysis evaluates the solar measurements in terms of instrument response rather than instrument gain, so an inverse F-factor is defined as

$$F_{\mathrm{Sun}}(\lambda,t) = \frac{1}{F(\lambda,t)} = \frac{R_{\mathrm{se}}^2(t)}{E_{\mathrm{sun}}(\lambda)} \times \frac{c_1(\lambda,t)\langle dn_{\mathrm{sd}}(\lambda,t)\rangle}{\mathrm{RVS}(\theta_{\mathrm{sd}},\lambda)\cos(\phi(t))\tau_{\mathrm{sds}}(\lambda)\mathrm{BRDF}(\lambda,t_0)} \times \frac{1}{NH(\lambda,t)}. \tag{13}$$

Figure 3 shows the solar calibration time series F_{Sun} derived for VIIRS. The solar diffuser time series uncorrected for diffuser BRDF changes is shown in Fig. 3(a). The overall effectiveness of the SDSM data in correcting the SD data for changes in diffuser BRDF is demonstrated by comparing the SD time series without corrections for diffuser BRDF changes [Fig. 3(a)] and the H-factors normalized by SDSM channel 8 [Fig. 1(b)] with the SD time series corrected for diffuser BRDF changes [Figs. 3(d) and 3(e)]. The flattening in the BRDF degradation trend in the latter part of the mission is a real effect that is observed in both the SD and SDSM time series and is removed by the BRDF correction of the SD time series.

The effectiveness of the three options for normalizing the H-factors that monitor the BRDF degradation is demonstrated in Fig. 3 for bands M1–M4. Unnormalized H-factors introduce periodic screen transmission function errors from the SDSM data into the solar time series, as shown in Fig. 3(b). H-factors normalized by SDSM channel 8 remove the periodic errors from the SDSM data but change the temporal dependence of the time series, as shown in Fig. 3(c). H-factors normalized by the detrended SDSM channel 8 remove the periodic errors SDSM data without changing the temporal dependence of the time series, as shown in Fig. 3(d). Comparison of these plots shows that normalization of the H-factors by SDSM channel 8 is necessary to minimize the noise in the solar calibration data. It will require the solar/lunar comparison to definitively determine if the detrended channel 8 normalization should be used. The size of the channel 8 detrending relative to the changes in radiometric response for band M5–M7 [Fig. 3(e)] precludes the use of these bands in this evaluation.

The OBPG minimizes any residual noise in the solar calibration by using fits to the BRDF-corrected solar diffuser time series in the calibration lookup tables. The OBPG has fit the F_{Sun} time series for bands M1–M4 with exponential plus linear functions of time,

$$f(\lambda,t) = A_0(\lambda) - A_1(\lambda)[1 - e^{-A_2(\lambda)(t-t_0)}] - A_3(\lambda)(t-t_0), \tag{14}$$

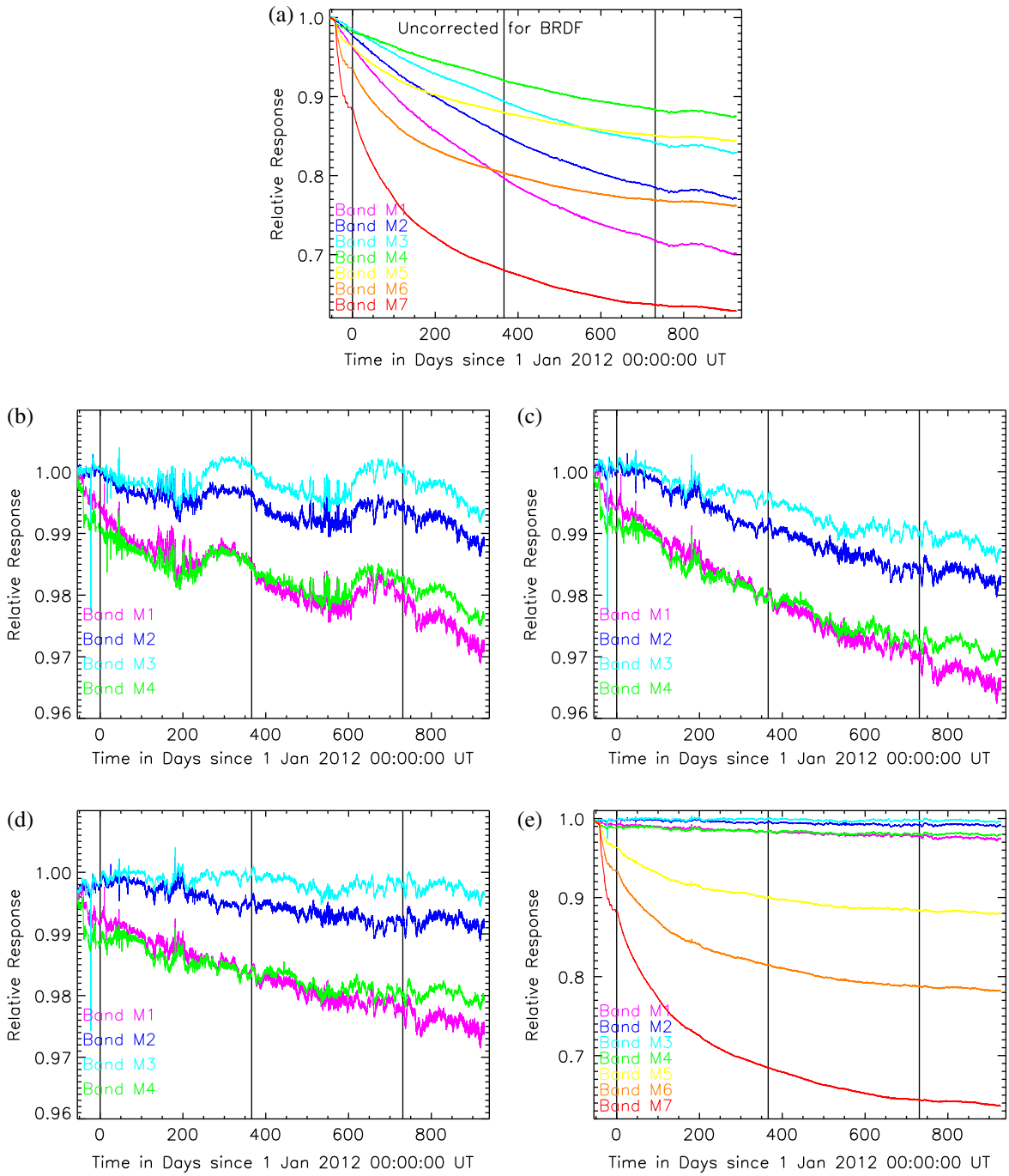

Fig. 3. Solar diffuser time series. (a) The trends for bands M1–M7, uncorrected for diffuser BRDF drift. (b) The trends for bands M1–M4, corrected for diffuser BRDF drift by unnormalized H-factors. (c) The trends for bands M1–M4, corrected for diffuser BRDF drift by H-factors normalized by SDSM channel 8. (d) The trends for bands M1–M4, corrected for diffuser BRDF drift by H-factors normalized by the detrended SDSM channel 8. (e) The trends for bands M1–M7, corrected for diffuser BRDF drift by H-factors normalized by the detrended SDSM channel 8. For clarity, these plots are shown for VIIRS detector 8.

and fits the time series for bands M5–M7 with simultaneous exponential functions of time,

$$f(\lambda,t) = A_0(\lambda) - A_1(\lambda)[1 - e^{-A_2(\lambda)(t-t_0)}] - A_3(\lambda)[1 - e^{-A_4(\lambda)(t-t_0)}]. \quad (15)$$

The fits of the solar calibration time series with the initial solar unit vectors and screen transmission functions, and the residuals of those fits, are shown in Fig. 4. The fits of the solar calibration time series with the updated solar unit vectors and revised screen transmission functions, and the residuals of those fits, are shown in Fig. 5. These two sets of figures clearly show the impact of the corrected solar unit vector reference frame and the corresponding revised screen transmission functions on the solar

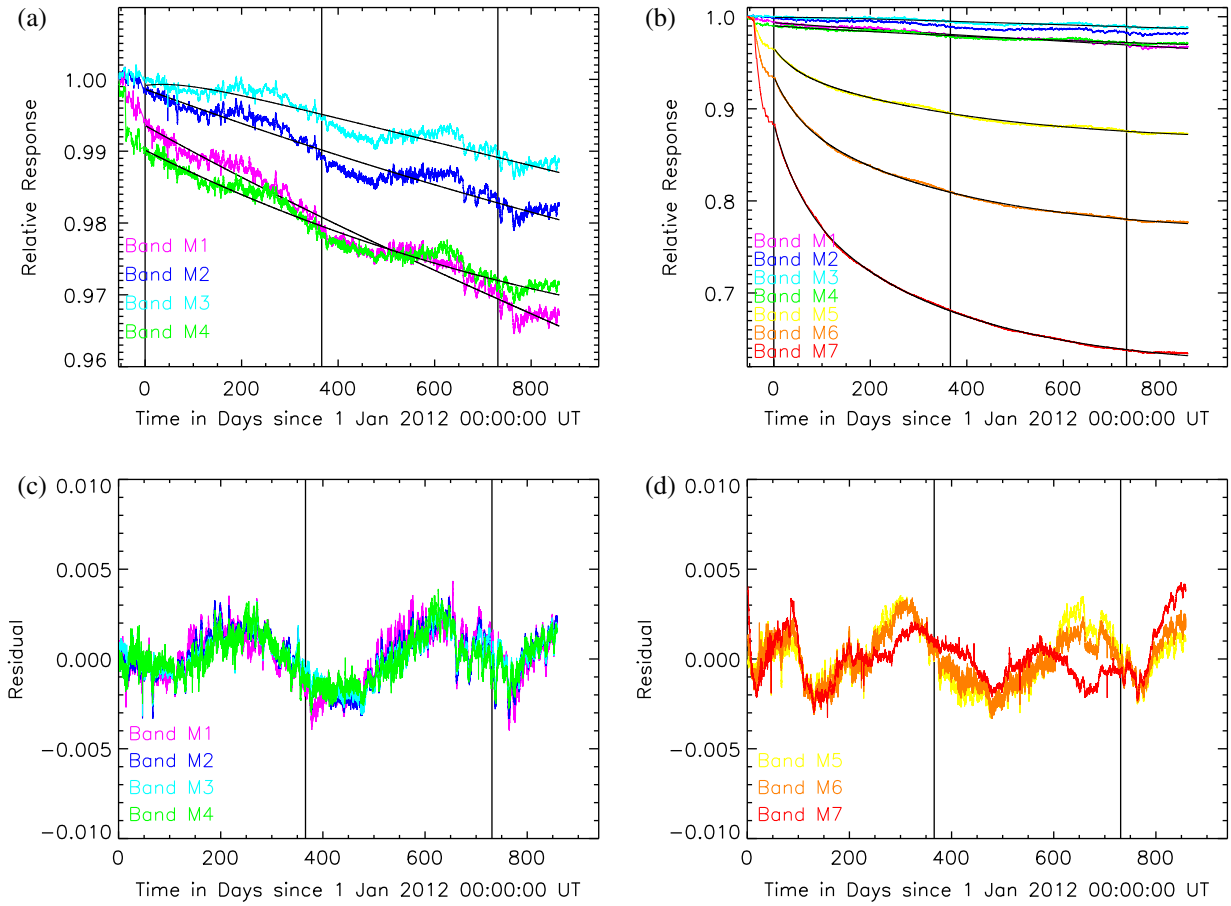

Fig. 4. Solar time series with initial solar unit vectors. Time series for the R2013.1 calibration, which were stopped when the updated screen transmission functions became available. (a) Exponential plus linear functions of time are fit for bands M1–M4. (b) Simultaneous exponential functions of time are fit for bands M5–M7. (c) Residuals of the fits for bands M1–M4. (d) Residuals of the fits for bands M5–M7.

calibration time series. For the blue bands (M1–M4) the dominant degradation mechanism is the diffuser BRDF degradation. Comparison of the residuals for these bands [Figs. 4(c) and 5(c)] shows that the revised residuals (for calibration R2014.0) are essentially flat and that the periodic signals observed in the initial residuals (for calibration R2013.1) have been removed. For the red bands (M5–M7) the dominant degradation mechanism is the NIR Degradation Anomaly. Comparison of the residuals for these bands [Figs. 4(d) and 5(d)] shows that the solar unit vector corrections and transmission screen updates did not significantly change the residuals for these bands (M5–M7).

The OBPG constructs the F-factor calibration lookup tables from inverses of fits to the F_{Sun} solar calibration time series, computed on a per-detector basis. The fits allow the F-factors to be extrapolated beyond the time of the last solar observation. These extrapolated F-factors allow the lookup tables to be used to process ocean color data in the forward data processing stream. During the time of the calibration extrapolation, additional solar and lunar observations are evaluated to determine when the lookup tables should be updated. When lookup table updates occur, the OBPG reprocesses the ocean data as needed to avoid discontinuities in the data product time series.

4. Lunar Calibration

The VIIRS lunar calibration procedure draws from MODIS heritage in that on an approximately monthly basis the SNPP spacecraft is rolled to observe the Moon through the space view at a target phase angle [24,43]. One difference from MODIS is that the VIIRS instrument design forces lunar observations to be obtained while the spacecraft is in the sunlight. Accordingly, possible observing geometries require spacecraft roll angles of 14° or less. Starting with the 2 April 2012 calibration, the target phase angle for lunar calibrations has been adjusted from −55° to −51° to meet thermal exclusion zone requirements. As was the case with MODIS, the Moon at times moves through the space view as the spacecraft/Moon geometries coincide, though the phase angle at these times is larger than the target phase angle. The OBPG uses these serendipitous lunar observations to supplement the scheduled lunar observations. The serendipitous observations may not provide full-disk lunar images for all of the bands because of the limited size of the space view. Because of the VIIRS lunar viewing geometry the Moon is below

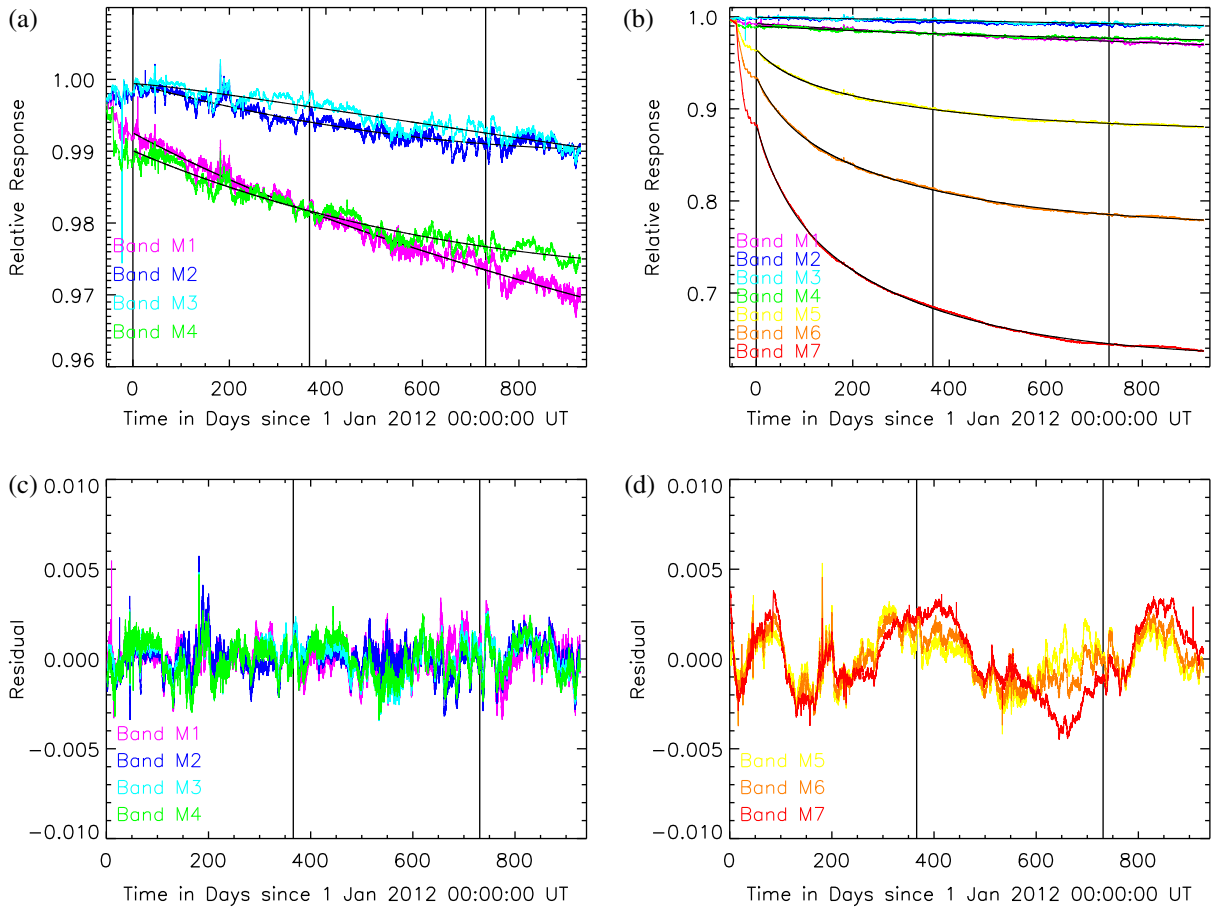

Fig. 5. Solar time series with corrected solar unit vectors. Time series for the R2014.0 calibration, which incorporates the solar unit vector coordinate frame correction and transmission screen updates. (a) Exponential plus linear functions of time are fit for bands M1–M4. (b) Simultaneous exponential functions of time are fit for bands M5–M7. (c) Residuals of the fits for bands M1–M4. (d) Residuals of the fits for bands M5–M7.

the Earth's horizon during lunar calibration opportunities for approximately three months out of the year during northern hemisphere summer [43]. Such annual gaps in lunar observations also occur for Terra MODIS and Aqua MODIS. Table 3 summarizes the lunar calibrations (22 scheduled and 5 serendipitous) observed so far by VIIRS and used by the OBPG in this analysis.

During a typical lunar maneuver, the spacecraft is rolled to observe the Moon through the space view at the target phase angle, the Moon drifts through the space view due to orbital motion of the spacecraft, then the spacecraft is rolled back to nadir pointing [24]. Figure 6 shows the sequence of lunar scans observed by band M4 during the 2 April 2012 lunar calibration as the Moon drifts through the space view. The ROLO model of the Moon requires disk-integrated lunar irradiance as input, so the OBPG only uses full-disk images from the lunar calibration scan sequence in computing band-averaged disk-integrated irradiance for each gain and mirror side of the calibration.

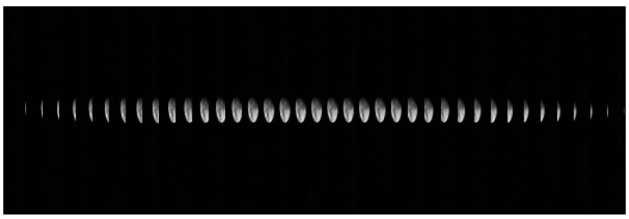

Fig. 6. Lunar calibration scan sequence. Band M4 scan sequence from the April 2012 lunar calibration.

A. Use of the ROLO Photometric Model of the Moon

The OBPG uses the USGS ROLO photometric model of the Moon [28,29] to normalize the lunar calibration time series for variations in observing geometry: instrument/Moon distances, Sun/Moon distances, and phase and libration angles. The disk-integrated lunar radiances are computed as

$$L_{\text{moon}}(\lambda, t) = \sum_{\text{pixels}} c_1(\lambda) dn_{\text{moon}}(\lambda, t), \tag{16}$$

where

$dn_{\text{moon}} \equiv$ dark-subtracted counts of the lunar pixels,
$c_1 \equiv$ linear counts-to-radiance conversion coefficient.

The ROLO model requires disk-integrated lunar irradiances as input, which are computed from the disk-integrated lunar radiances and the instantaneous field of view (IFOV) of VIIRS:

$$E_{\text{inst}}(\lambda, t) = \text{IFOV}_{\text{along-scan}}\text{IFOV}_{\text{along-track}}L_{\text{moon}}(\lambda, t), \tag{17}$$

where

$\text{IFOV}_{\text{along-scan}} \equiv 0.3104$ mrad for dual-gain M bands,
$\text{IFOV}_{\text{along-track}} \equiv 0.9313$ mrad for all bands.

The radiometric output of the model is the ratio of the irradiances measured by VIIRS to the irradiances predicted by the model (E_{rolo}):

$$F_{\text{Moon}}(\lambda, t) = \frac{E_{\text{inst}}(\lambda, t)}{E_{\text{rolo}}(\lambda, t)}. \tag{18}$$

B. Impact of Modulated Relative Spectral Responses on Lunar Data

To evaluate the impact of the time-varying (modulated) relative spectral responses on the lunar data, the OBPG compared the solar and lunar calibrations directly on an observation-by-observation basis, using the solar observations that are closest in time to the lunar observations. Typically, the coincident solar and lunar observations occur within 30 min. The lunar observations used in this analysis have been corrected for the residual sub-spacecraft point libration effects, as will be discussed in Section 4.C. For the comparison, the OBPG normalized the lunar time series for each band by a factor that minimizes the differences between the individual lunar and solar calibrations over the mission.

The details of the RSR analysis for band M1 are shown in Fig. 7. Figure 7(a) shows the relative spectral response for band M1 at the time of the first lunar calibration (January 2012) and at the time of the last lunar calibration to date (July 2014). The change in the RSR over time is its modulation. Note that there is a significant change in the longer-wavelength part of the RSR between these two times. The NIR Degradation Anomaly caused the change in the "red leak" of the RSR with time: the degradation of the instrument response in the near infrared causes the size of the out-of-band signal on the red side of the band pass to change relative to the in-band signal [26,27]. This change in the out-of-band

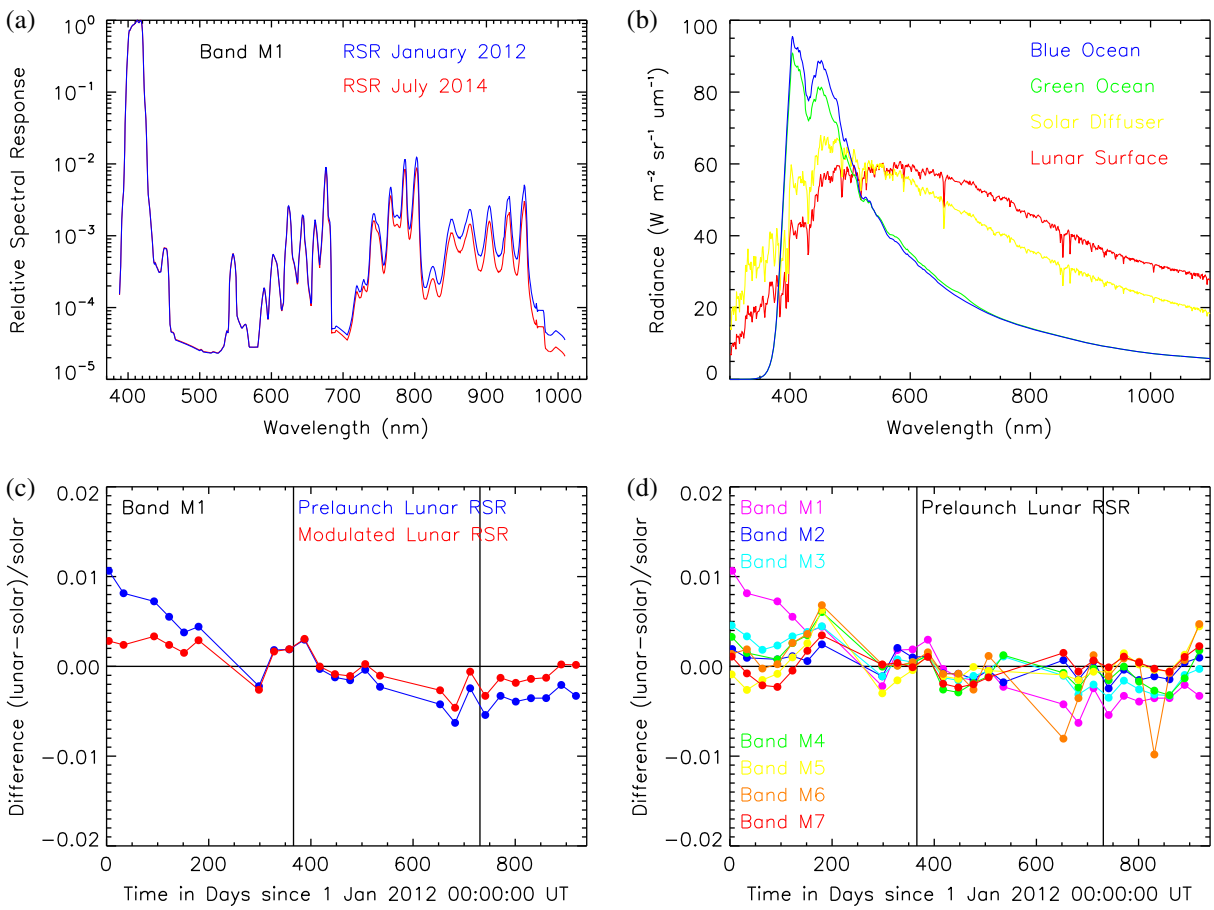

Fig. 7. Modulated relative spectral responses for band M1. (a) The first RSR is shown in blue, while the last RSR is shown in red. (b) Reference TOA spectra for evaluating relative spectral responses. (c) Band M1 solar and lunar comparisons. (d) Solar and lunar comparisons for bands M1–M7 using prelaunch RSRs for the lunar data.

signal is modeled as a change in the RSR overtime. The TOA reference spectra for a blue ocean, a green ocean, the solar diffuser, and the lunar surface are shown in Fig. 7(b). The differences in these source spectral shapes give rise to the various impacts of the changing red leak on the VIIRS radiometric response. For this analysis, VCST provided a modulated RSR for the VIIRS bands at the time of each lunar calibration.

Figure 7(c) shows the band M1 solar/lunar calibration comparison using the prelaunch RSR for both the solar and lunar data (in blue) and shows the comparison using the prelaunch RSR for the solar data and the modulated RSR for the lunar data (in red). A third comparison used the modulated RSR for both solar data and lunar data, but this comparison was indistinguishable from the second comparison using the modulated RSR for the lunar data alone. The modulated RSR affects the lunar data but not the solar data due to the redder spectral shape of the lunar spectrum compared to the solar diffuser spectrum, as shown in Fig. 7(b). The modulated RSR has no impact on the ocean data because the blue and green ocean spectra have much smaller red components than do the solar diffuser and lunar spectra.

Figure 7(d) shows the solar/lunar calibration comparison for bands M1–M7 with the prelaunch RSRs used for the lunar data. Band M1 is out of family in the comparison with bands M2–M7 due to the changing red leak in that band. Figure 10(a) shows the solar/lunar comparison using the modulated RSRs for the lunar data, where band M1 is now in family. Comparison of Fig. 7(d) and Fig. 10(a) shows that the impact of the modulated RSRs is 1% for band M1, 0.1% for band M2, and negligible for bands M3–M7.

C. Lunar-Derived Radiometric Response Trends

Figure 8 shows the relative radiometric responses for bands M1–M7, normalized to the first lunar calibration. These data were processed with the modulated relative spectral responses. As initially reported for the R2013.1 VIIRS calibration [17], the current lunar analysis confirms that the periodic signals in the lunar time series are correlated with sub-spacecraft point librations [Figs. 8(e) and 8(f)]. These periodic signals can be characterized by residuals of fits of simultaneous exponential functions of time to the lunar time series for bands M1–M4 [shown in Fig. 8(a)] and for bans M5–M7 [shown in Fig. 8(e)]. Correlations between the residuals of these fits and the sub-spacecraft libration points are shown in Table 4. The correlations are stronger for bands M1–M4 than for bands M5–M7. Sufficient lunar observations have been obtained by this point to verify that the ROLO model output has wavelength-dependent sub-spacecraft point libration dependencies. To account for these dependencies, the OBPG fit the lunar time series computed from ROLO model output, and derived from Eq. (18), with simultaneous exponential functions of time plus linear functions of the longitude and latitude of the sub-spacecraft point. The fits have the form

$$f(\lambda, t, \delta, \gamma) = A_0(\lambda) - A_1(\lambda)[1 - e^{-\tau_1(t-t_0)}] - A_2(\lambda)(t - t_0)[1 - e^{-\tau_2(t-t_0)}] + A_3(\lambda)\delta + A_4(\lambda)\gamma, \tag{19}$$

where

$\tau_i \equiv$ time constants of the exponential functions,
$\delta \equiv$ longitude of the sub-spacecraft point,
$\gamma \equiv$ latitude of the sub-spacecraft point.

For bands M1–M4, the optimum fits were obtained for a short-period time constant of 100 days and a long-period time constant of 400 days. For bands M5–M7, the optimum fits were obtained for a short-period time constant of 40 days and a long-period time constant of 100 days. The differences in the time constants arise from the dominant radiometric response degradation mechanisms for the respective wavelength regions. For the blue bands (M1–M4) the dominant degradation is yellowing of the half-angle mirror and other telescope optics as has been observed with heritage instruments [13,44,45]. For the red bands (M5–M7) the dominant degradation is the NIR Degradation Anomaly. The exponential fit coefficients and time constants are shown in Table 5, while the libration coefficients are shown in Table 6.

Examination of the fit residual plots in Fig. 9 shows that there are no periodic signals in the residuals. The noise appears to arise from observational scatter. The larger scatter in the observations for band M6, compared to that observed for bands M1–M5 and M7, arises from the increased uncertainties in determining disk-integrated irradiances for bands which undergo along-scan aggregation on orbit. These results verify the supposition [17] that, while the ROLO model provides a wavelength-independent sub-spacecraft point libration correction for lunar observations [28,29], the ROLO output has wavelength-dependent sub-spacecraft point libration dependencies. The next version of the ROLO model will incorporate the wavelength-dependent sub-spacecraft point libration corrections to account for this effect [46]. It should be noted that the periodic signals in the lunar time series have also been seen by VCST [47] and NOAA NESDIS/STAR [18] without the underlying cause of these signals being identified.

The OBPG uses the ROLO-derived lunar calibration time series, computed with the modulated RSRs and corrected for the residual sub-spacecraft point libration effects, as the second monitor of the VIIRS radiometric response over time. As with the solar data analysis, the lunar data is evaluated in terms of instrument response:

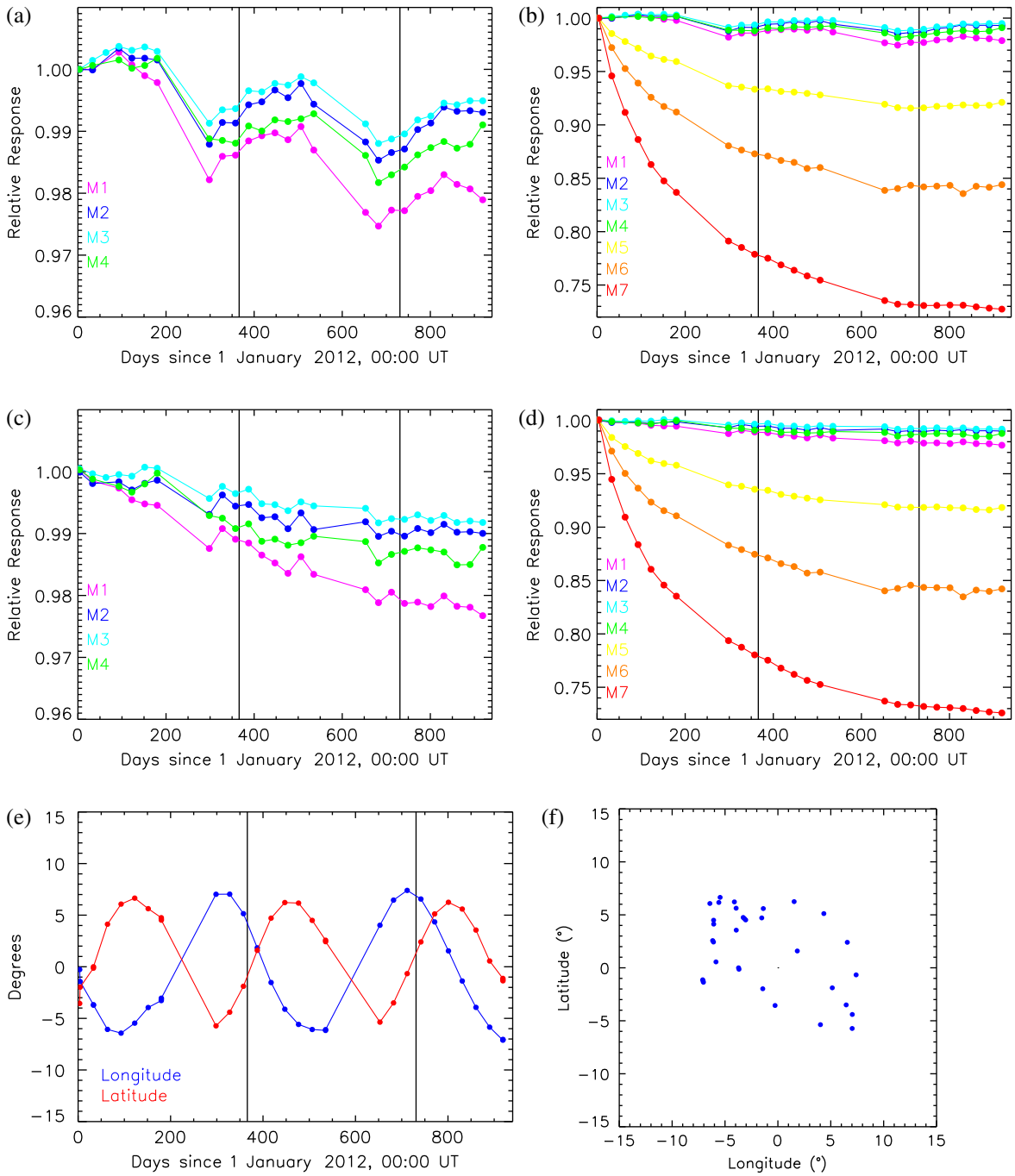

Fig. 8. Lunar calibration time series. (a) The trends for bands M1–M4. (b) The trends for bands M1–M7. (c) The trends for bands M1–M4, corrected for the libration of the sub-spacecraft point. (d) The trends for bands M1–M7, corrected for the libration of the sub-spacecraft point. (e) The sub-spacecraft point libration time series. (f) The sub-spacecraft point libration spatial distribution.

$$F_{\text{Moon}}(\lambda, t, \delta, \gamma, \text{RSR}) = \frac{E_{\text{inst}}(\lambda, t)}{E_{\text{rolo}}(\lambda, t, \text{RSR})}[1 - K_{\text{lib-lon}}(\lambda)\delta] \times [1 - K_{\text{lib-lat}}(\lambda)\gamma], \tag{20}$$

where

$K_{\text{lib-lon}} \equiv$ sub-spacecraft point longitude libration correction [A_3 of Eq. (19)]
$K_{\text{lib-lat}} \equiv$ sub-spacecraft point latitude libration correction [A_4 of Eq. (19)].

The lunar time series shown in Eq. (20) is the ratio of the VIIRS observations to the ROLO model predictions [Eq. (18), with modulated RSRs added as input to the ROLO model], corrected for the libration effects derived from the sub-spacecraft point libration fits in Eq. (19). These libration corrections are provided in Table 6, along with the relative size of the libration corrections for each band. The corrections range from 1% for bands M1 and M2 to 0.8%

Table 3. Lunar Calibrations[a]

Cal Date	Number	Cal Type	Bands	Gains	Phase
4 January 2012	1	Roll	M3–M7	hi,lo	−55.4
5 January 2012	1	Serendipitous	M1–M3	hi,lo	−44.5
3 Febrary 2012	1	Roll	M1–M11	hi,lo	−56.8
4 March 2012	1	Serendipitous	M3, M5–M11	hi,lo	−48.9
2 April 2012–31 May 2012	3	Roll/Sector	M1–M11	hi	−51.7
28 June 2012	1	Serendipitous	M1–M11	hi,lo	−65.7
25 October 2012–21 May 2013	8	Roll/Sector	M1–M11	hi	−50.8
19 June 2013	1	Serendipitous	M1–M4, M8,M9,M11	hi,lo	−56.6
14 October 2013–9 June 2014	9	Roll/Sector	M1–M11	hi	−51.8
7 July 2014	1	Serendipitous	M1–M11	hi,lo	−61.8

[a]The VIIRS lunar calibrations obtained through July 2014. Sector denotes calibrations where the data collection for scans in the space view were rotated into the Earth view to provide band coregistration.

Table 4. Lunar Fit Residual/Sub-Spacecraft Point Libration Correlations[a]

Band	λ (nm)	Longitude	Latitude
M1	412	−0.838	0.831
M2	445	−0.885	0.767
M3	488	−0.908	0.713
M4	555	−0.873	0.631
M5	672	−0.800	0.504
M6	746	−0.545	0.404
M7	865	−0.645	0.522

[a]Correlations are shown between residuals of fits to the lunar time series for bands M1–M7 and the longitude and latitude of the sub-spacecraft points.

for bands M3 and M4 to 0.6% for bands M5–M7, showing the wavelength dependence of the residual libration effect in the lunar time series. The lunar calibration time series, corrected for the residual sub-spacecraft point libration, are shown in Fig. 8. The libration-corrected lunar time series provides a long-term stable calibration reference for VIIRS.

5. Lunar Adjustment of Solar Calibration Trends

In assessing the uncertainties in the solar calibration time series, a primary concern is how effectively the SDSM tracks the solar diffuser BRDF degradation. Since the Moon is a more stable calibration reference than the solar diffuser [30], the OBPG has compared the solar time series to the lunar time series to identify any extraneous trends in the solar data. As was discussed for the modulated RSR analysis, the OBPG compared the solar and lunar calibrations directly on an observation-by-observation basis:

$$\Delta F(\lambda,t) = \left(N_{\mathrm{MS}}(\lambda)\frac{F_{\mathrm{Moon}}(\lambda,t,\delta,\gamma,\mathrm{RSR})}{F_{\mathrm{Moon}}(\lambda,t_0,\delta_0,\gamma_0,\mathrm{RSR}_0)} - \frac{F_{\mathrm{Sun}}(\lambda,t)}{F_{\mathrm{Sun}}(\lambda,t_0)}\right)\Big/\left(\frac{F_{\mathrm{Sun}}(\lambda,t)}{F_{\mathrm{Sun}}(\lambda,t_0)}\right), \tag{21}$$

where F_{Sun} is defined by Eq. (13), F_{Moon} is defined by Eq. (20), and N_{MS} is a normalization that minimizes the differences between the individual lunar and solar calibrations over the mission. Likely causes of trends between the solar and lunar time series could be inhomogeneous degradation of the diffuser BRDF [19] or changes in the center wavelengths of the SDSM channels.

As was discussed in Section 3, the OBPG identified three options for normalizing the H-factors that monitor the diffuser BRDF degradation. The OBPG has finalized the evaluation of these options by comparing the solar and lunar calibrations directly using ΔF, as shown in Fig. 10:

(1) Figure 10(a) shows the comparison using unnormalized H-factors for the solar data.

(2) Figure 10(b) shows the comparison using H-factors normalized by SDSM channel 8 for the solar data.

(3) Figure 10(c) shows the comparison using H-factors normalized by the detrended SDSM channel 8 [shown in Fig. 2(b)] for the solar data.

(4) Figure 10(d) shows the comparison using H-factors normalized by the detrended SDSM channel 8 and the lunar-derived temporal adjustments that will be discussed later in this section.

Table 5. Lunar Exponential Fit Coefficients[a]

Band	λ (nm)	A_0	A_1	A_2	τ_1	τ_2
M1	412	0.999308	0.008798	−0.033531	0.0100	0.0025
M2	445	0.999278	0.003506	−0.014524	0.0100	0.0025
M3	488	0.999602	0.006101	−0.015511	0.0100	0.0025
M4	555	1.000078	0.004068	−0.020619	0.0100	0.0025
M5	672	1.000827	−0.012774	−0.075483	0.0250	0.0100
M6	746	1.004675	−0.034524	−0.138775	0.0250	0.0100
M7	865	1.010494	−0.078416	−0.218010	0.0250	0.0100

[a]The exponential fit coefficients and time constants of Eq. (19) are provided. The time constants have units of days^{-1}.

Table 6. Sub-Spacecraft Point Libration Corrections[a]

Band	λ (nm)	Longitude ($K_{\text{lib-lon}}$)	Latitude ($K_{\text{lib-lat}}$)	Size of Correction (%)
M1	412	−0.000409	0.000461	1.0929
M2	445	−0.000492	0.000312	1.0308
M3	488	−0.000482	0.000177	0.85643
M4	555	−0.000492	0.000121	0.80444
M5	672	−0.000424	0.0000233	0.61297
M6	746	−0.000338	0.000115	0.59000
M7	865	−0.000314	0.000161	0.61219

[a]The lunar time series linear fit coefficients for the sub-spacecraft longitude and latitude libration effects $K_{\text{lib-lon}}$ is coefficient A_3 and $K_{\text{lib-lat}}$ is coefficient A_4 of Eq. (19). The relative size of the correction for each band in provided.

These plots show the impact of the channel 8 normalization options on the residual time trends in the solar time series. Comparison of Figs. 10(a) and 10(b) shows that the channel 8 normalization reduces the noise in the solar time series, while introducing a time trend in the data. This effect was also observed in the solar data analysis (Fig. 3). Comparison of Figs. 10(b) and 10(c) shows that using the detrended channel 8 normalization minimizes the noise in the solar time series without introducing a residual time trend. This comparison shows that the detrended SDSM channel 8 normalization should be used, which is a distinction that could not be made using the solar data alone. Accordingly, the OBPG has adopted the detrended channel 8 time series to normalize the H-factors that are then used to correct the diffuser degradation in the solar time series.

To identify any extraneous trends in the solar data, the OBPG assessed the significance of the slopes in the solar and lunar calibration comparison for Fig. 10(c) by performing the following statistical analysis for each band:

(1) Compute a linear fit to the differences between the solar and lunar calibrations (as defined by ΔF).
(2) Compute the t-statistics for the differences between the solar and lunar calibrations (as defined by ΔF).
(3) Compute the p-values based on the t-statistics, assuming the null hypothesis of the slope being indistinguishable from zero at the ~1% level.
(4) Determine the statistical significance of the slopes based on whether or not the null hypothesis holds true.

The results of this statistical analysis are summarized in Table 7. A direct comparison of the radiometric trends between the solar and lunar time series

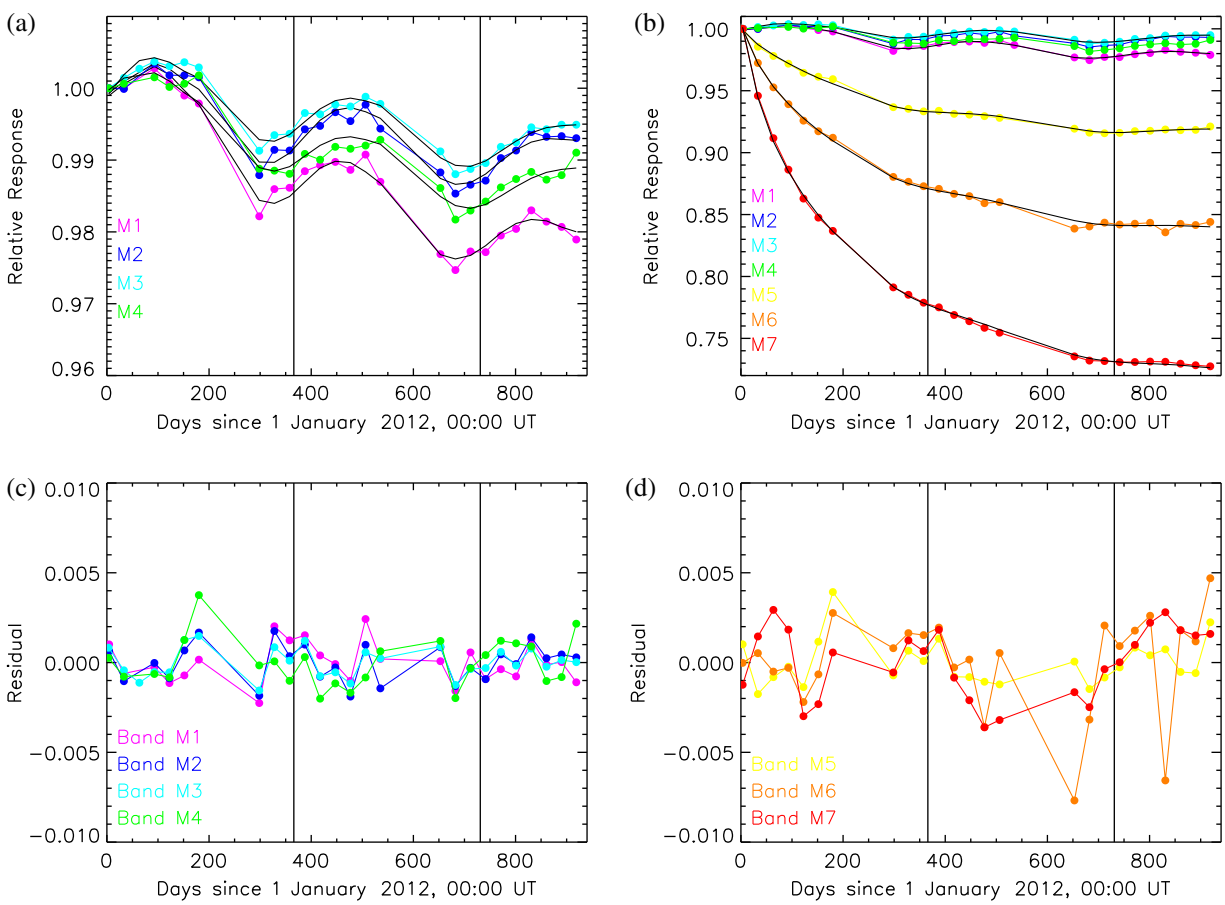

Fig. 9. Fits to lunar calibration time series. Simultaneous exponential functions of time plus linear functions of sub-spacecraft longitude and latitude are fit to the time series. (a) The fits for bands M1–M4. (b) The fits for bands M1–M7. (c) Residuals of the fits for bands M1–M4. (d) Residuals of the fits for bands M5–M7.

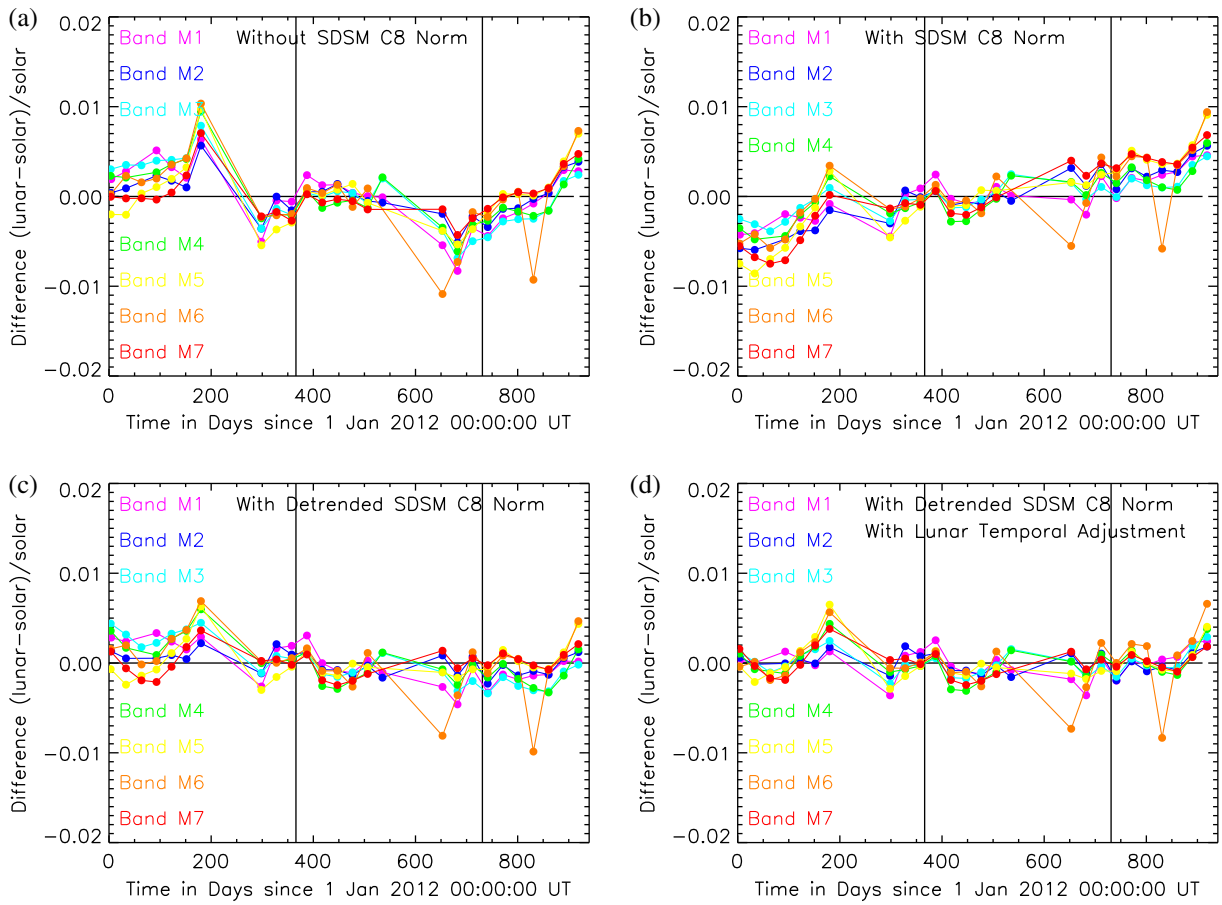

Fig. 10. Solar and lunar calibration comparisons for bands M1–M7. (a) Comparison using unnormalized H-factors for the solar data. (b) Comparison using H-factors normalized by SDSM channel 8 for the solar data. (c) Comparison using H-factors normalized by the detrended SDSM channel 8 for the solar data. (d) Comparison using H-factors normalized by the detrended SDSM channel 8 and the lunar-derived temporal adjustments for the solar data. The lunar data incorporate sub-spacecraft point libration corrections and modulated relative spectral response functions.

Table 7. Solar/Lunar Trend Comparisons[a]

Band	λ (nm)	Slope (ΔF_1)	t-Statistic	P-Value	$\mathrm{Log}_{10}(P)$	Significant	Rev Slope
M1	412	−5.21E − 06	−4.53	0.0001517	−3.82	Yes	1.60E − 08
M2	445	−1.83E − 06	−2.26	0.0332675	−1.48	No	1.52E − 09
M3	488	−6.87E − 06	−7.41	0.0000001	−6.92	Yes	2.56E − 08
M4	555	−5.23E − 06	−4.07	0.0004690	−3.33	Yes	1.64E − 08
M5	672	7.02E − 07	0.49	0.6259058	−0.20	No	−1.36E − 11
M6	746	−4.26E − 06	−1.90	0.0701247	−1.15	No	1.09E − 08
M7	865	6.05E − 07	0.59	0.5588272	−0.25	No	−8.39E − 13

[a]The table summarizes the statistical analysis of the solar/lunar calibration comparison for Fig. 10(c). The end results of the analysis are determinations of significance for the slopes. For the final lunar-adjusted solar and lunar calibrations shown in Fig. 10(d), the slopes of the comparison are provided in the final column.

show differences of 0.3% for band M1, of 0.4% for band M3, and of 0.3% for band M4. The OBPG has used these trends between the solar and lunar time series to adjust the SDSM-corrected solar time series for bands M1, M3, and M4 to match the temporal response of the lunar time series:

$$F_{\mathrm{Sun}}^{\mathrm{Adj}}(\lambda, t) = (1 + \Delta F_1(\lambda)(t - t_0))F_{\mathrm{Sun}}(\lambda, t), \qquad (22)$$

where ΔF_1 is the slope of the difference between the solar and lunar calibrations, the ΔF. The resulting comparisons between the lunar-adjusted solar time series and the lunar time series are shown in Fig. 10(d) and the slopes of these comparisons are shown in the final column of Table 7. This comparison is the current best estimate of the differences between the solar and lunar calibration time series. Since the statistical analysis of the solar/lunar comparison shows that the slopes for bands M1, M3,

and M4 are significant, the OBPG has derived the F-factors for the R2014.0 VIIRS calibration from inverses of fits to the lunar-adjusted solar calibration time series $F_{\mathrm{Sun}}^{\mathrm{Adj}}$, using the fitting functions defined by Eq. (14) for bands M1–M4 and Eq. (15) for bands M5–M7.

6. Detector and Mirror Side Relative Responses

Variations in detector response across a band can give rise to striping in ocean color products. In a similar fashion, variations in the half-angle mirror side response for a band can give rise to banding in ocean color products. To minimize these striping and banding effects, the OBPG computed relative detector responses across each band and mirror side relative responses for each band from the solar diffuser observations. The OBPG has used lunar data to validate the solar-derived detector and mirror side relative responses. For both analyses, the solar observations have had the time-dependent radiometric corrections applied [using Eq. (22)], but the lunar observations have not had the radiometric corrections applied. In the analysis that follows, the solar and lunar data (for a detector or mirror side) for a given observation are normalized by mean values (over detectors or mirror sides) of that observation, so the radiometric corrections to the solar data minimize differences in the detector responses over time for the solar observations.

In the detector analysis, for every solar observation the radiometric response for each detector was normalized to the mean radiometric responses over the detectors of that band, yielding the detector relative response for the band and observation. The relative detector-to-detector responses for each band do not change over time, indicating that they define a radiometric characteristic of each band. Consequently, the responses for each band were averaged over the mission. Figure 11 shows the detector responses for bands M1–M7. For the lunar observations, the OBPG derived a single-detector lunar image for every detector in each band (see Fig. 6). For each observation, lunar images were extracted from the data for each detector. The integrated radiances for these single-detector images were normalized by the mean of the integrated radiances for all of the detectors in each band, yielding the detector response for each band and observation. The responses were averaged over the mission, and are also shown in Fig. 11. Overall, the detector responses derived

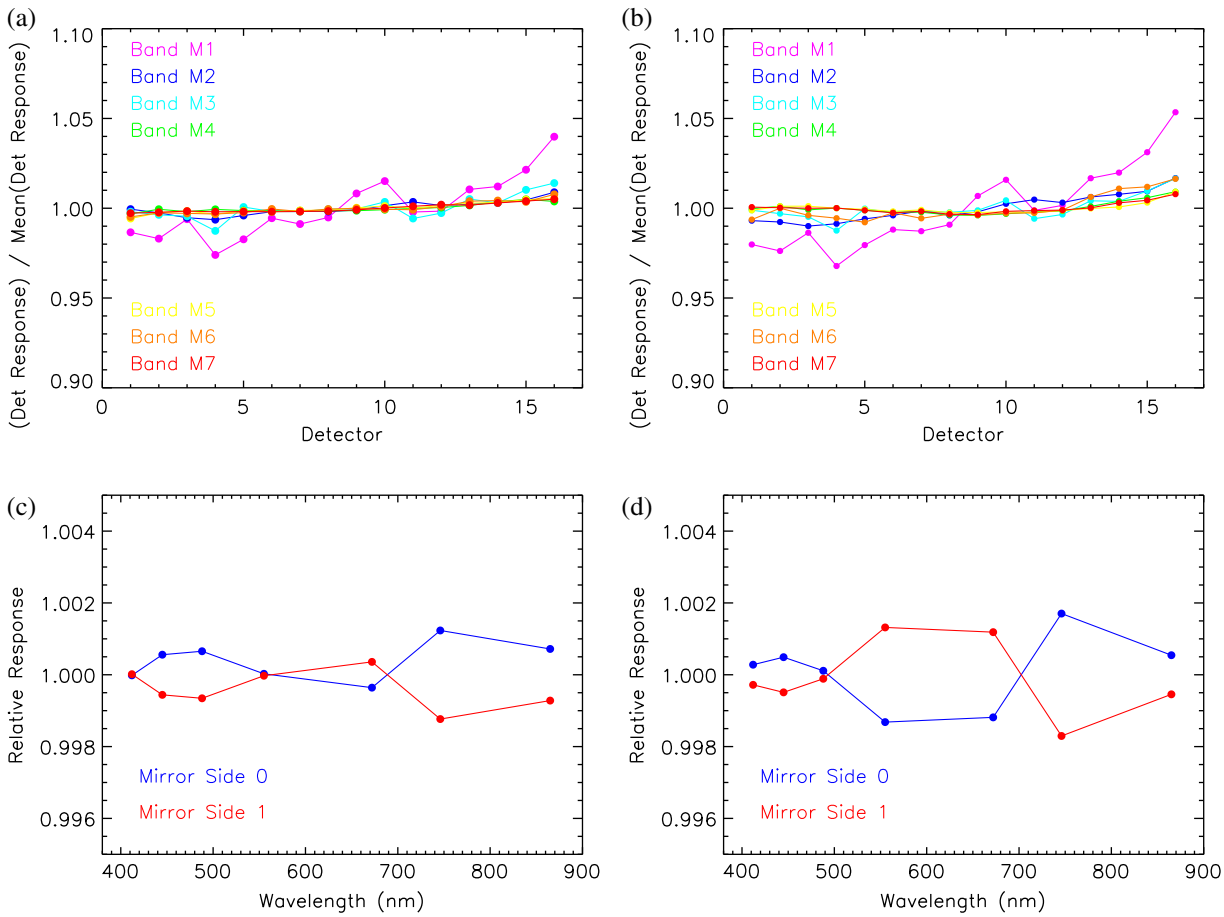

Fig. 11. Detector and mirror side relative responses. (a) Detector relative responses from solar data. (b) Detector relative responses from lunar data. (c) Mirror side relative responses from solar data. (d) Mirror side relative responses from lunar data. The lunar data have not had the detector-dependent radiometric corrections applied.

from the lunar data verify the detector responses derived from the solar data. Both data sets show that band M1 exhibits the strongest trend in detector response across the band.

In the mirror side analysis, for every solar observation the radiometric response is averaged over detectors for each mirror side and normalized to the mean response of the two mirror sides, yielding the mirror side response for each band and observation. The mirror side responses for each band do not change over time, indicating that they define a radiometric characteristic for each band. Consequently, the responses for each band were averaged over the mission. Figure 11 shows the mirror side responses for bands M1–M7. For the lunar observations, the ROLO model outputs for each mirror side were normalized to the mean of the ROLO outputs for the two mirror sides, yielding the mirror side response for the band and observation. The responses were averaged over the mission, and are also shown in Fig. 11. Overall, the mirror side responses derived from the lunar data verify the mirror side responses derived from the solar data. While the solar data show significant mirror side differences for bands M6 and M7, the lunar data also show significant differences for bands M4 and M5.

The solar diffuser data provide a more frequent (once per orbit) and less noisy determination of both the detector and mirror side relative responses than do the lunar data. Accordingly, the OBPG has incorporated detector and mirror side responses derived from the solar diffuser data into the VIIRS F-factor calibration lookup tables.

7. Uncertainties in the On-Orbit Calibration of VIIRS

An initial assessment of uncertainties in the on-orbit calibration of VIIRS was afforded by comparing residuals of fits to the solar time series (Fig. 5) with residuals of fits to the lunar time series (Fig. 9). The OBPG generally chooses the simplest fitting function that models the instrument behavior for calibration time series analysis. To date, the solar time series for bands M1–M4 have been fit with exponential plus linear functions of time, while the solar time series for bands M5–M7 and the lunar time series for bands M1–M7 have been fit with simultaneous exponential functions of time. Consequently, the solar time series for bands M1–M4 have also been fit with simultaneous exponential functions of time to provide a consistent comparison for this uncertainty analysis. Figure 12 shows this comparison. For the solar and lunar comparison, the magnitudes and

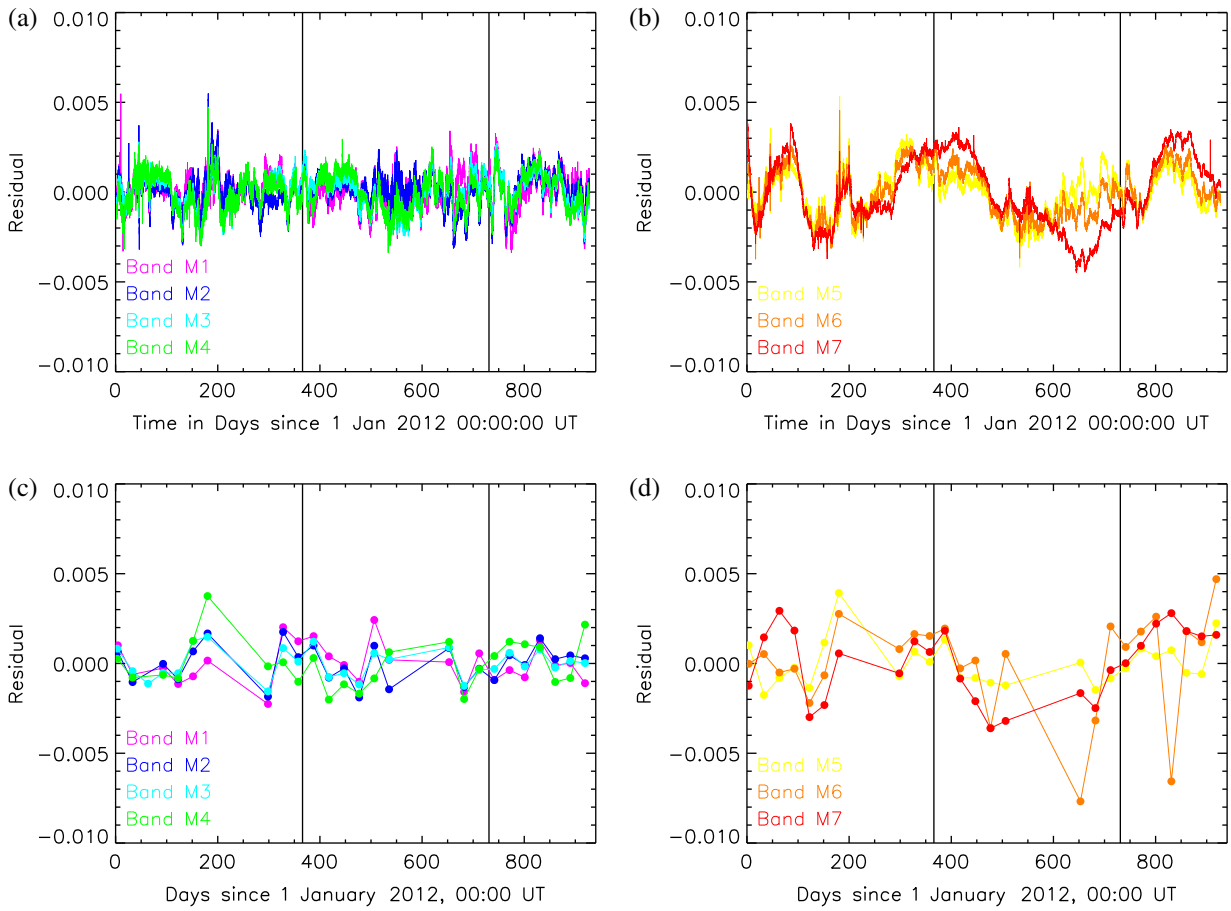

Fig. 12. Solar and lunar residual comparison. The fitting functions are simultaneous exponential functions of time. (a) Solar calibration residuals for bands M1–M4. (b) Solar calibration residuals for bands M5–M7. (c) Lunar calibration residuals for bands M1–M4. (d) Lunar calibration residuals for band M5–M7.

overall behavior of the residuals for bands M1–M4 are comparable, as are those for bands M5–M7, which implies that the residuals for the two data sets arise from the same radiometric behavior of the instrument. The detailed comparisons of the solar and lunar residuals do not show any statistically significant correlations in the two residual data sets.

A more rigorous comparison of the solar and lunar calibration time series have allowed the OBPG to refine the uncertainties in the VIIRS on-orbit calibration, as are summarized in Table 8. The solar calibration time series shows uncertainties (mean residuals) per band of 0.067%–0.17%, the lunar calibration time series shows uncertainties (mean residuals) per band of 0.069%–0.20%, and the relative differences in the two on-orbit calibrations are 0.093%–0.22%. These uncertainties are comparable to the mission-long uncertainties of 0.033%–0.13% determined for SeaWiFS [13] and better than the mission-long uncertainties of 0.38%–0.94% determined for Terra MODIS lunar observations [48] and of 0.30%–0.58% determined for Aqua MODIS lunar observations [48].

A final consideration in this analysis is one of using the lunar-adjusted solar calibration time series to derive the F-factors for ocean data processing versus using the lunar calibration time series alone for this purpose. There are several factors that argue for using the lunar-adjusted solar calibrations:

(1) Because lunar observations are acquired on a monthly basis, several years of lunar calibrations are required to obtain a sufficient sample size to discern long-term radiometric trends in the lunar data. To date, 22 scheduled and 5 serendipitous lunar calibrations have been observed by VIIRS. The OBPG used 79 lunar calibrations acquired over more than 6 years to derived the first definitive on-orbit calibration for SeaWiFS [49]. Currently, the VIIRS lunar time series has only 1/3 the observations as the SeaWiFS lunar time series used for the first definitive calibration.

(2) The solar calibration data provide a detector-specific calibration of VIIRS. The lunar observations do not readily lend themselves to a per detector calibration.

Table 8. On-Orbit Calibration Uncertainty[a]

Band	λ (nm)	Solar Cal Uncertainty (%)	Lunar Cal Uncertainty (%)	Relative Differences (%)
M1	412	0.0739	0.0875	0.119
M2	445	0.0671	0.0863	0.093
M3	488	0.0791	0.0690	0.106
M4	555	0.0831	0.106	0.137
M5	672	0.101	0.0996	0.146
M6	746	0.118	0.200	0.224
M7	865	0.168	0.171	0.115

[a]The relative uncertainties are the mean residuals for the solar and lunar calibrations. The solar/lunar calibration drifts are means from the time series of Fig. 10.

(3) The reliability of the long-term radiometric trends from the solar data is ultimately limited by our understanding of the degradation of the solar diffuser. As the number of lunar calibrations increase with time, the lunar data provide a more stable long-term radiometric reference than does the solar data.

For these reasons, the OBPG has used the lunar-adjusted solar calibration time series to derive the F-factor lookup table used for the R2014.0 VIIRS calibration. It should be noted here that calibration uncertainties are only one component of the total uncertainties in top-of-the-atmosphere radiances. Eplee *et al.* (2012) [13] provide a more thorough discussion of the relationship between calibration uncertainties and uncertainties in TOA radiances.

8. Calibration Validation

The calibration of any ocean color satellite instrument should provide stable calibrated TOA radiances that can be used for the retrieval of ocean color data products. The ultimate validation of the on-orbit calibration resides with a time series analysis of the retrieved ocean color data products. To validate the current VIIRS on-orbit calibration, the OBPG compared two versions of the VIIRS ocean color data products:

(1) Products from global mission Reprocessing R2013.1 [22], which used the R2013.1 calibration of VIIRS [17], including the lunar libration correction for the sub-spacecraft longitude and the first on-orbit update of the screen transmission functions based on yaw maneuver data by VCST [36].

(2) Products from global mission Reprocessing R2014.0 [22], which used the R2014.0 calibration of VIIRS, including the lunar libration correction for both the sub-spacecraft longitude and latitude, the modulated relative spectral responses [26,27] for the lunar data, the screen transmission functions updated for the corrected solar unit vectors and additional yaw maneuver and flight data by VCST [25], and the lunar-derived adjustments for bands M1, M3, and M4.

The results of this calibration validation analysis are shown in Fig. 13, where anomaly plots of remote sensing reflectances for bands M1–M6 and chlorophyll concentration are compared. An anomaly plot is a multiyear plot of the average of a geophysical parameter where the average annual trend in the parameter has been subtracted. These analyses were performed for retrievals over deep water, with a depth of 1000 m or more. The input data for the analyses were monthly global composites of the remote sensing reflectances or chlorophyll generated over the mission. The comparisons show that the R2014.0 calibration significantly reduces the secular trends in the anomaly plots over those obtained for the R2013.1 calibration. The calibration validation shows the VIIRS R2014.0 calibration has met its primary purpose of allowing the retrieval of more stable

ocean color data products than was possible using the R2013.1 calibration.

9. Discussion of Results

Based on its experience with SeaWiFS, Terra MODIS, and Aqua MODIS, the OBPG has developed two independent monitors of the VIIRS on-orbit radiometric response using solar diffuser and lunar observations obtained through July 2014. Working to minimize the differences between these two calibration data sets has allowed the OBPG to identify refinements for both. Specific improvements to the on-orbit calibration implemented by the OBPG for the reflective solar bands include:

Prelaunch Calibration

(1) Linearization of the counts-to-radiance conversion coefficients for the expected range of TOA radiances for bands M1–M7 to increase calibration consistency at low radiance levels.

Solar Calibration

(2) Conversion of solar unit vectors to the J2000 reference frame for the solar calibration data and for the screen transmission functions (0.4% effect for bands M1–M4).

(3) Detrended SDSM channel 8 (935 nm) normalization of the H-factors (detrending is a 1.3% effect, noise correction through normalization is a 1% effect).

(4) Interpolation of the SDSM-derived H-factors to the time basis of the solar calibrations, allowing direct correction of the F-factors by the interpolated H-factors.

Lunar Calibration

(5) Use of modulated RSRs for the lunar data to account for changes in the out-of-band responses (1% effect in band M1, 0.1% effect in band M2, no discernible effect in bands M3–M7).

(6) Wavelength-dependent libration corrections for the sub-spacecraft point longitudes and latitudes (1% effect in bands M1 and M2, 0.8% effect in bands M3 and M4, 0.6% effect in bands M5–M7).

Solar and Lunar Calibration Comparison

(7) Lunar-derived trend adjustments for the solar calibration time series (0.3% effect in band M1, 0.4% effect in band M3, 0.3% effect in band M4).

(8) Exponential plus linear functions of time fit to the final adjusted solar time series for bands M1–M4. Simultaneous exponential functions of time fit to the final adjusted solar time series for bands M5–M7.

Of the various research groups that are pursuing the on-orbit calibration of VIIRS, only the OBPG is making full use of both the solar and lunar calibration data sets. Additionally, the OBPG is the only group that has implemented the detrended SDSM channel 8 normalization of the H-factors for the solar calibration data and the sub-spacecraft point libration corrections for the lunar calibration data. The detrended SDSM channel 8 normalization reduces the observational noise and residual solar incidence angle effects in SDSM channels 1–7 without altering the time trends in the data. Using the interpolated H-factors to track the solar diffuser BRDF changes allows for correction of residuals in the solar diffuser data that are also observed by the SDSM. The sub-spacecraft point libration correction to the lunar data allows the adjustments to bands M1, M3, and M4 to be computed. Delaying fits until the final adjusted solar calibration time series is derived allows the OBPG to minimize the noise in the final radiometric response trends while minimizing artifacts that may be introduced into the time series. While these calibrations are retrospective in nature and rely on the ability of the Ocean Data Processing System to readily reprocess the mission-long VIIRS ocean data set, extrapolation of the fits into the future allows the calibration lookup tables to be used for processing ocean data in the forward stream. The fits that are incorporated into the calibration lookup tables are extrapolated for 180 days beyond the time of the last solar observation, providing calibration projections beyond the annual gaps in the lunar observations.

A. Calibration Equation Summary

The on-orbit calibration that the OBPG applies to VIIRS Earth data is built up from a series of analyses of on-orbit SDSM, solar calibration, and lunar calibration observations. The solar and lunar data analyses run in parallel, then the results are compared to produce the final radiometric calibration for the instrument.

Changes in the solar diffuser BRDF are tracked through H-factors derived from SDSM measurements:

$$h(\lambda,t) = \frac{\langle dn_{\mathrm{sd}}(\lambda,t)\rangle}{\langle dn_{\mathrm{sun}}(\lambda,t)\rangle}\frac{\cos(\phi(t))\tau_{\mathrm{sdsm}}(\lambda)}{\tau_{\mathrm{sds}}(\lambda)\mathrm{BRDF}(\lambda,t_0)\Omega_{\mathrm{sdsm}}}. \quad (23)$$

The diffuser BRDF corrections are normalized by SDSM channel 8:

$$NH(\lambda,t) = K_{c8}(t)\frac{h(\lambda,t)}{h(\lambda,t_0)}\frac{h_{c8}(t_0)}{h_{c8}(t)}. \quad (24)$$

The solar-derived instrument radiometric response is corrected for the changing diffuser BRDF:

$$F_{\mathrm{Sun}}(\lambda,t) = \frac{R_{\mathrm{se}}^2(t)}{E_{\mathrm{sun}}(\lambda)} \times \frac{c_1(\lambda,t)\langle dn_{\mathrm{sd}}(\lambda,t)\rangle}{\mathrm{RVS}(\theta_{\mathrm{sd}},\lambda)\cos(\phi(t))\tau_{\mathrm{sds}}(\lambda)\mathrm{BRDF}(\lambda,t_0)} \times \frac{1}{NH(\lambda,t)}. \quad (25)$$

Disk-integrated lunar irradiances are computed from the lunar calibration images:

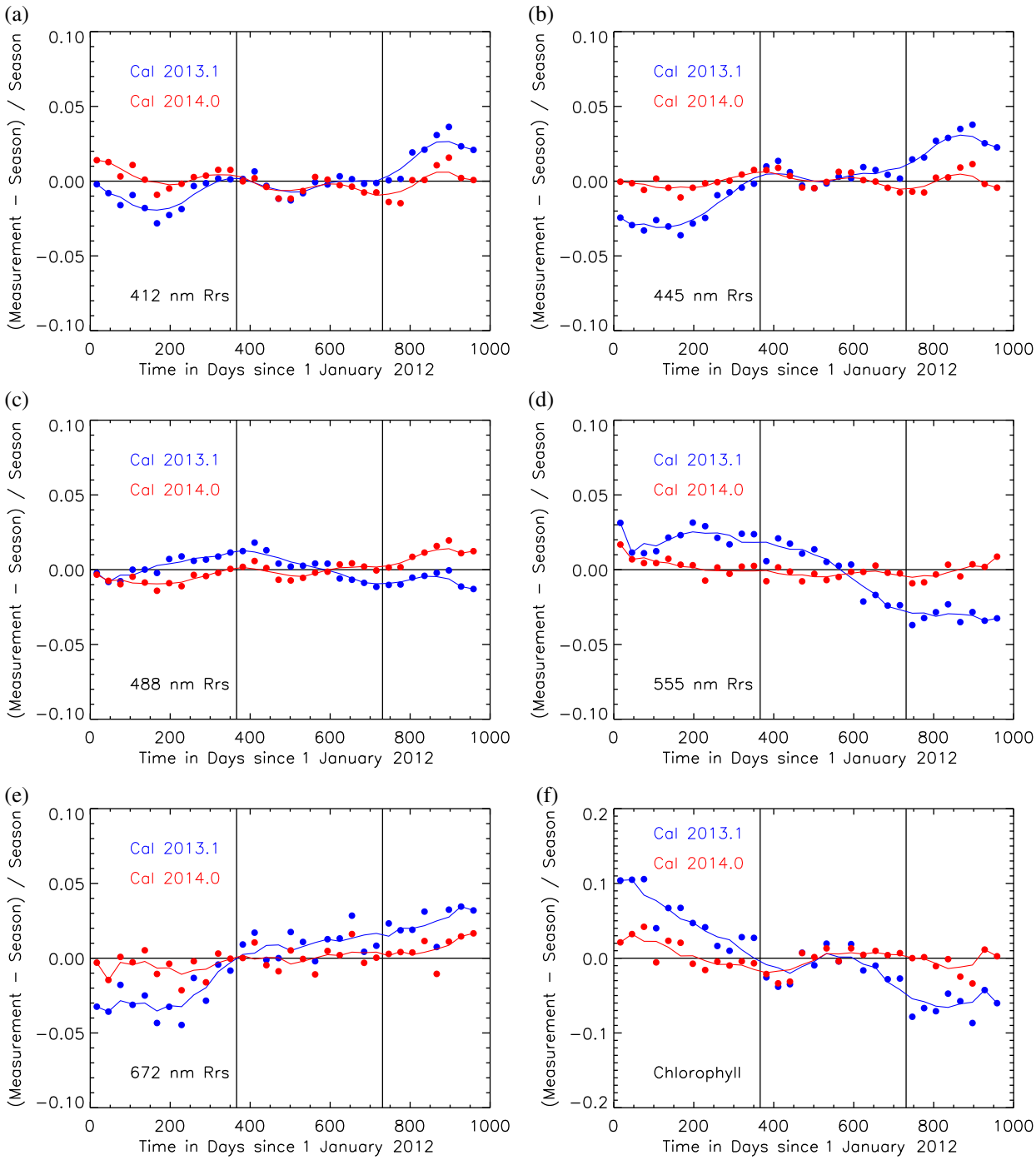

Fig. 13. VIIRS ocean color product comparisons. Anomaly plots of VIIRS ocean color products for deep water derived with the existing and revised instrument calibrations are compared. (a) Remote sensing reflectance for band M1 (412 nm). (b) Remote sensing reflectance for band M2 (445 nm). (c) Remote sensing reflectance for band M3 (488 nm). (d) Remote sensing reflectance for band M4 (555 nm). (e) Remote sensing reflectance for band M6 (672 nm). (f) Chlorophyll A concentration. The 2014 calibration (shown in red) improves the ocean color product time series (Reprocessing R2014.0) over those of the 2013 calibration (shown in blue) ocean color product time series (Reprocessing R2013.1).

$$E_{\text{inst}}(\lambda,t) = \text{IFOV}_{\text{along-scan}}\text{IFOV}_{\text{along-track}} \times \sum_{\text{pixels}} c_1(\lambda) dn_{\text{moon}}(\lambda,t). \tag{26}$$

The lunar-derived instrument radiometric response is corrected for sub-spacecraft point librations:

$$F_{\text{Moon}}(\lambda,t,\delta,\gamma,\text{RSR}) = \frac{E_{\text{inst}}(\lambda,t)}{E_{\text{rolo}}(\lambda,t,\text{RSR})}[1-K_{\text{lib-lon}}(\lambda)\delta] \times [1-K_{\text{lib-lat}}(\lambda)\gamma]. \tag{27}$$

Comparison of the solar and lunar radiometric responses allows extraneous trends in the solar time series to be identified:

$$\Delta F(\lambda,t) = \left(N_{\mathrm{MS}}(\lambda)\frac{F_{\mathrm{Moon}}(\lambda,t,\delta,\gamma,\mathrm{RSR})}{F_{\mathrm{Moon}}(\lambda,t_0,\delta_0,\gamma_0,\mathrm{RSR}_0)} - \frac{F_{\mathrm{Sun}}(\lambda,t)}{F_{\mathrm{Sun}}(\lambda,t_0)}\right) \Big/ \left(\frac{F_{\mathrm{Sun}}(\lambda,t)}{F_{\mathrm{Sun}}(\lambda,t_0)}\right). \tag{28}$$

The F-factors incorporated into the VIIRS calibration lookup tables are computed from inverses to fits of the lunar-adjusted solar calibration time series:

$$F_{\mathrm{Sun}}^{\mathrm{Adj}}(\lambda,t) = (1 + \Delta F_1(\lambda)(t - t_0))F_{\mathrm{Sun}}(\lambda,t). \tag{29}$$

B. Application of the On-Orbit Calibration

The improvements in the solar and lunar calibrations discussed above have brought the solar and lunar radiometric trends for VIIRS into close agreement. Fits to the solar calibrations show mean residuals per band of 0.066%–0.17%, while fits to the lunar calibrations show mean residuals per band of 0.069%–0.20%. Comparison of the VIIRS solar and lunar time series (Figs. 10 and 12) shows that the relative differences in the two calibrations are 0.093%–0.22% (Table 8). The magnitudes and overall behavior of the residuals for the blue bands (M1–M4) are comparable, as are those for the red bands (M5–M7). Most of the calibration artifacts have been corrected in the data and the residuals for the two data sets arise from observational scatter. The uncertainties in the VIIRS calibration are comparable to the mission-long uncertainties of 0.033%–0.13% determined for SeaWiFS [13] and to the mission-long uncertainties of 0.38%–0.94% determined for Terra MODIS lunar observations [48] and of 0.30%–0.58% determined for Aqua MODIS lunar observations [48]. Since measurements of the Moon are more stable over time than are measurements of the solar diffuser [30], the OBPG has used the solar/lunar calibration comparison (Table 7) to adjust the time trends in the solar data to match the temporal response of the lunar data. A calibration lookup table for VIIRS reprocessing R2014.0 has been generated from fits to the adjusted solar calibration time series. The impact of the uncertainties in the calibration on the VIIRS long-term ocean color data record has been reported elsewhere by the OBPG [50].

The goal of the on-orbit calibration of an ocean color satellite instrument is the production of stably calibrated TOA radiances, from which ocean color data products can be retrieved for climate change research [51]. By analyzing both the solar and lunar calibration data sets, the OBPG has achieved a radiometric stability for the VIIRS on-orbit calibration that is commensurate with those achieved for SeaWiFS and Aqua MODIS, supporting the incorporation of VIIRS data into the long-term NASA ocean color data record [52].

The authors wish to thank Ning Lei and Boryana Efremova of VCST for providing us with the updated SDSM and SD screen transmission and diffuser BRDF functions. In addition, Ning Lei provided us with the modulated relative spectral responses for VIIRS. The authors wish to thank Tom Stone of the U.S. Geological Survey for running the OBPG-derived disk-integrated lunar irradiance through the ROLO photometric model in a timely manner and for discussions concerning the residual libration effects in the ROLO model output.

References

1. J. C. Cardema, K. W. Rausch, N. Lei, D. I. Moyer, and F. J. DeLuccia, "Operational calibration of VIIRS reflective solar band sensor data records," Proc. SPIE **8510**, 851019 (2012).
2. C. Cao, F. J. De Luccia, X. Xiong, R. Wolfe, and F. Weng, "Early on-orbit performance of the Visible Infrared Imaging Radiometer Suite onboard the Suomi National Polar-Orbiting Partnership (S-NPP) Satellite," IEEE Trans. Geosci. Remote Sens. **52**, 1142–1156 (2014).
3. C. Cao, J. Xiong, S. Blonski, Q. Liu, S. Uprety, X. Shao, Y. Bai, and F. Weng, "Suomi NPP VIIRS sensor data record verification, validation, and long-term performance monitoring," J. Geophys. Res. Atmos. **118**, 11644–11678 (2013).
4. N. Lei, Z. Wang, J. Fulbright, S. Lee, J. McIntire, K. Chiang, and X. Xiong, "Initial on-orbit radiometric calibration of the Suomi NPP VIIRS reflective solar bands," Proc. SPIE **8510**, 851018 (2012).
5. X. Xiong, J. Butler, K. Chaing, B. Efremova, J. Fulbright, N. Lei, J. McIntire, H. Oudrari, J. Sun, Z. Wang, and A. Wu, "VIIRS on-orbit calibration methodology and performance," J. Geophys. Res. Atmos. **119**, 5065–5078 (2014).
6. F. De Luccia, D. Moyer, E. Johnson, K. Rausch, N. Lei, K. Chiang, X. Xiong, J. Fulbright, E. Haas, and G. Iona, "Discovery and characterization of on-orbit degradation of the Visible Infrared Imaging Radiometer Suite (VIIRS) Rotating Telescope Assembly (RTA)," Proc. SPIE **8510**, 85101A (2012).
7. J. D. Barrie, P. D. Fuqua, M. J. Meshishnek, M. R. Ciofalo, C. T. Chu, J. A. Chaney, R. M. Moision, and L. Graziani, "Root cause determination of on-orbit degradation for the VIIRS Rotating Telescope Assembly," Proc. SPIE **8510**, 85101B (2012).
8. S. Blonski and C. Cao, "Monitoring and predicting rate of VIIRS sensitivity degradation from telescope contamination by tungsten oxide," Proc. SPIE **8739**, 87390D (2013).
9. B. A. Franz, S. W. Bailey, G. Meister, and P. J. Werdell, "Quality and consistency of the NASA ocean color data record," in *Proc. Ocean Optics XXI*, Glasgow, Scotland, 8–12 October 2012.
10. National Research Council, *Climate Data Records from Environmental Satellites: Interim Report* (The National Academies, 2004).
11. C. R. McClain, W. E. Esaias, W. Barnes, B. Guenther, D. Endres, S. B. Hooker, G. Mitchell, and R. Barnes, in *SeaWiFS Calibration and Validation Plan*, NASA Tech. Memo. S. B. Hooker and E. R. Firestone, eds. (NASA Goddard Space Flight Center, 1992), Vol. **3**, p. 104566.
12. H. R. Gordon, "Atmospheric correction of ocean color imagery in the Earth Observing System era," J. Geophys. Res. **102**, 17081–17106 (1997).
13. R. E. Eplee, Jr., G. Meister, F. S. Patt, R. A. Barnes, S. W. Bailey, B. A. Franz, and C. R. McClain, "On-orbit calibration of SeaWiFS," Appl. Opt. **51**, 8702–8730 (2012).
14. B. A. Franz, S. W. Bailey, P. J. Werdell, and C. R. McClain, "Sensor-independent approach to the vicarious calibration of satellite ocean color radiometry," Appl. Opt. **46**, 5068–5082 (2007).
15. M. Wang, X. Liu, L. Tan, L. Jiang, S.-H. Son, W. Shi, K. Rausch, and K. Voss, "Impacts of VIIRS SDR performance on ocean color products," J. Geophys. Res. Atmos. **118**, 10347–10360 (2013).
16. R. E. Eplee, Jr., K. R. Turpie, G. F. Fireman, G. Meister, T. C. Stone, F. S. Patt, B. A. Franz, S. W. Bailey, W. D. Robinson, and C. R. McClain, "VIIRS on-orbit calibration for ocean color data processing," Proc. SPIE **8510**, 85101G (2012).

17. R. E. Eplee, Jr., K. R. Turpie, G. Meister, F. S. Patt, G. F. Fireman, B. A. Franz, and C. R. McClain, "A synthesis of VIIRS solar and lunar calibrations," Proc. SPIE **8866**, 88661L (2013).
18. J. Sun and M. Wang, "VIIRS reflective solar bands on-orbit calibration and performance: a three-year update," Proc. SPIE **9264**, 92640L (2014).
19. J. Sun and M. Wang, "Visible Infrared Imaging Radiometer Suite solar diffuser calibration and its challenges using a solar diffuser stability monitor," Appl. Opt. **53**, 8571–8584 (2014).
20. J. Sun, M. Wang, L. Tan, and L. Jiang, "An efficient approach for VIIRS RDR to SDR data processing," IEEE Geosci. Remote Sens. Lett. **11**, 2037–2041 (2014).
21. J. Sun and M. Wang, "On-orbit characterization of the VIIRS solar diffuser and solar diffuser screen," Appl. Opt. **54**, 236–252 (2015).
22. The NASA Ocean Color Data Reprocessing page, available at http://oceancolor.gsfc.nasa.gov/cms/reprocessing.
23. J. Sun and X. Xiong, "Solar and lunar observation planning for Earth-observing sensor," Proc. SPIE **8176**, 817610 (2011).
24. J. J. Butler, X. Xiong, R. A. Barnes, F. S. Patt, J. Sun, and K. Chiang, "An overview of Suomi NPP VIIRS calibration maneuvers," Proc. SPIE **8510**, 85101J (2012).
25. N. Lei, X. Chen, and X. Xiong, "Determination of the SNPP VIIRS SDSM screen transmittance from both yaw maneuver and regular on-orbit data," Proc. SPIE **9218**, 921803 (2014).
26. N. Lei, B. Guenther, Z. Wang, and X. Xiong, "Modeling SNPP VIIRS reflective solar bands optical throughput degradation and its impacts on the relative spectral response," Proc. SPIE **8866**, 88661H (2013).
27. N. Lei, X. Xiong, and B. Guenther, "Modeling the detector radiometric gains of the Suomi NPP VIIRS reflective solar bands," IEEE Trans. Geosci. Remote Sens. **53**, 1565–1573 (2015).
28. H. H. Kieffer and T. C. Stone, "The spectral irradiance of the Moon," Astron. J. **129**, 2887–2901 (2005).
29. T. C. Stone and H. H. Kieffer, "Use of the Moon to support on-orbit sensor calibration for climate change measurements," Proc. SPIE **6296**, 62960Y (2006).
30. H. H. Kieffer, "Photometric stability of the lunar surface," Icarus **130**, 323–327 (1997).
31. D. K. Clark, H. R. Gordon, K. J. Voss, Y. Ge, W. Broenkow, and C. Trees, "Validation of atmospheric correction over the oceans," J. Geophys. Res. **99**, 7293–7307 (1997).
32. D. K. Clark, M. E. Feinholz, M. A. Yarbrough, B. C. Johnson, S. W. Brown, Y. S. Kim, and R. A. Barnes, "Overview of the radiometric calibration of MOBY," Proc. SPIE **4483**, 64–76 (2002).
33. Z. Ahmad, B. A. Franz, C. R. McClain, E. J. Kwiatkowska, J. Werdell, E. P. Shettle, and B. N. Holben, "New aerosol models for the retrieval of aerosol optical thickness and normalized water-leaving radiances from the SeaWiFS and MODIS sensors over coastal regions and open oceans," Appl. Opt. **49**, 5545–5560 (2010).
34. K. Rausch, S. Houchin, J. Cardema, G. Moy, E. Haas, and F. J. De Luccia, "Automated calibration of the Suomi National Polar-Orbiting Partnership (S-NPP) Visible Infrared Imaging Radiometer Suite (VIIRS) reflective solar bands," J. Geophys. Res. Atmos. **118**, 13434–13442 (2013).
35. D. Moyer, N. Vandermierden, K. Rausch, and F. De Luccia, "VIIRS reflective solar bands on-orbit calibration coefficient performance using imagery and moderate band intercomparisons," Proc. SPIE **9223**, 922305 (2014).
36. J. McIntire, B. Efremova, D. Moyer, S. Lee, and X. Xiong, "Analysis of Suomi-NPP VIIRS vignetting functions based on yaw maneuver data," Proc. SPIE **8510**, 85101K (2012).
37. J. P. Fulbright, N. Lei, K. Chiang, and X. Xiong, "Characterization and performance of the Suomi-NPP VIIRS solar diffuser stability monitor," Proc. SPIE **8510**, 851015 (2012).
38. J. P. Fulbright, N. Lei, J. McIntire, B. Efremova, X. Chen, and X. Xiong, "Improving the characterization and performance of the Suomi-NPP VIIRS solar diffuser stability monitor," Proc. SPIE **8866**, 88661J (2013).
39. X. Xiong, R. E. Eplee, Jr., J. Sun, F. S. Patt, A. Angal, and C. R. McClain, "Characterization of MODIS and SeaWiFS solar diffuser on-orbit degradation," Proc. SPIE **7452**, 74520Y (2009).
40. R. E. Eplee, Jr., F. S. Patt, R. A. Barnes, and C. R. McClain, "SeaWiFS long-term solar diffuser reflectance and sensor noise analyses," Appl. Opt. **46**, 762–773 (2007).
41. X. Xiong, X. Xie, A. Angal, J. Choi, J. Sun, and W. L. Barnes, "Characterization of MODIS solar diffuser on-orbit degradation," Proc. SPIE **6677**, 6670O (2007).
42. G. Georgiev and J. J. Butler, "Long-term calibration monitoring of Spectralon diffusers BRDF in the air-ultarviolet," Appl. Opt. **46**, 7892–7899 (2007).
43. F. S. Patt, R. E. Eplee, R. A. Barnes, G. Meister, and J. J. Butler, "Use of the Moon as a calibration reference for NPP VIIRS," Proc. SPIE **5882**, 588215 (2005).
44. X. Xiong, J. Sun, W. Barnes, V. Salomonson, J. Esposito, H. Erives, and B. Guenther, "Multiyear on-orbit calibration and performance of Terra MODIS reflective solar bands," IEEE Trans. Geosci. Remote Sens. **45**, 879–889 (2007).
45. X. Xiong, J. Sun, X. Xie, W. L. Barnes, and V. V. Salomonson, "On-orbit calibration and performance of Aqua MODIS reflective solar bands," IEEE Trans. Geosci. Remote Sens. **48**, 535–546 (2010).
46. T. C. Stone, private communication (2014).
47. J. P. Fulbright, Z. Wang, and X. Xiong, "Suomi-NPP VIIRS lunar radiometric calibration observations," Proc. SPIE **9218**, 921804 (2014).
48. R. E. Eplee, Jr., J.-Q. Sun, G. Meister, F. S. Patt, X. Xiong, and C. R. McClain, "Cross calibration of SeaWiFS and MODIS using on-orbit observations of the Moon," Appl. Opt. **50**, 120–133 (2011).
49. R. E. Eplee, Jr., R. A. Barnes, F. S. Patt, G. Meister, and C. R. McClain, "SeaWiFS lunar calibration methodology after six years on orbit," Proc. SPIE **5542**, 1–13 (2004).
50. K. R. Turpie, R. E. Eplee, Jr., B. A. Franz, and C. Del Castillo, "Calibration uncertainty in ocean satellite sensors and trends in long-term environmental records," Proc. SPIE **9111**, 91103 (2014).
51. C. R. McClain and G. Meister, eds., "Mission requirements for future ocean-colour sensors," Reports of the International Ocean-Color Coordinating Group, No. 13 (IOCCG, 2012).
52. C. R. McClain, "A decade of satellite ocean color observations," Annu. Rev. Mar. Sci. **1**, 19–42 (2009).